

UKAEA-CCFE-PR(18)54

O. Linder, J. Citrin, G.M.D. Hogeweyj, C. Angioni, C. Bourdelle, F.J. Casson, E. Fable, A. Ho, F. Koechl, M. Sertoli, the EUROfusion MST1 Team and the ASDEX Upgrade Team

# **Flux-driven integrated modelling of main ion pressure and trace tungsten transport in ASDEX Upgrade**

Enquiries about copyright and reproduction should in the first instance be addressed to the  
UKAEA  
Publications Officer, Culham Science Centre, Building K1/0/83 Abingdon, Oxfordshire,  
OX14 3DB, UK. The United Kingdom Atomic Energy Authority is the copyright holder.

# **Flux-driven integrated modelling of main ion pressure and trace tungsten transport in ASDEX Upgrade**

O. Linder, J. Citrin, G.M.D. Hogeweij, C. Angioni, C. Bourdelle, F.J.  
Casson, E. Fable, A. Ho, F. Koechl, M. Sertoli, the EUROfusion  
MST1 Team and the ASDEX Upgrade Team



# Flux-driven integrated modelling of main ion pressure and trace tungsten transport in ASDEX Upgrade

O. Linder<sup>1,2</sup>, J. Citrin<sup>1</sup>, G.M.D. Hogewij<sup>1</sup>, C. Angioni<sup>3</sup>, C. Bourdelle<sup>4</sup>, F.J. Casson<sup>5</sup>, E. Fable<sup>3</sup>, A. Ho<sup>1</sup>, F. Koechl<sup>6</sup>, M. Sertoli<sup>3</sup>, the EUROfusion MST1 Team\* and the ASDEX Upgrade Team

<sup>1</sup>DIFFER - Dutch Institute for Fundamental Energy Research, De Zaale 20, 5612 AJ Eindhoven, the Netherlands

<sup>2</sup>Eindhoven University of Technology, De Zaale, 5612 AJ Eindhoven, the Netherlands

<sup>3</sup>Max-Planck-Institut für Plasmaphysik, Boltzmannstraße 2, D-85748 Garching, Germany

<sup>4</sup>CEA, IRFM, F-13108 Saint-Paul-lez-Durance, France

<sup>5</sup>CCFE, Culham Science Centre, Abingdon, Oxon, OX14 3DB, UK

<sup>6</sup>ÖAW/ATI, Atominstytut, TU Wien, 1020 Vienna, Austria

\***See author list of Meyer et al.** "Overview of progress in European Medium Sized Tokamaks towards an integrated plasma-edge/wall solution", *Nucl. Fusion* **57**, 102014 (2017).

**Abstract.** Neoclassical and turbulent heavy impurity transport in tokamak core plasmas are determined by main ion temperature, density and toroidal rotation profiles. Thus, in order to reproduce experimental behaviour of W accumulation, integrated modelling of main ion heat and particle transport is a vital prerequisite. For the first time, the quasilinear gyrokinetic code QuaLiKiz has been applied for successful predictions of core kinetic profiles in an ASDEX Upgrade H-mode discharge in the turbulence dominated region within the integrated modelling suite JETTO. Neoclassical contributions are calculated by NCLASS; auxiliary heat and particle deposition profiles due to NBI and ECRH prescribed from previous analysis with TRANSP. Turbulent and neoclassical contributions are insufficient in explaining main ion heat and particle transport inside the  $q = 1$  surface, necessitating the prescription of further transport coefficients to mimic the impact of MHD activity on central transport. The ion to electron temperature ratio at the simulation boundary stabilizes ion scale modes while destabilizing ETG modes when significantly exceeding unity. Careful analysis of experimental measurements using Gaussian process regression techniques is carried out to apply reasonable values. In following trace W impurity transport simulations performed with additionally NEO, neoclassical transport under consideration of poloidal asymmetries alone is found to be insufficient to establish hollow central W density profiles. Reproduction of these conditions measured experimentally is found possible only when assuming the direct impact of a saturated  $(m, n) = (1, 1)$  MHD mode on heavy impurity transport.

## 1 Introduction

In a future commercial fusion reactor, key requirements for the materials used in plasma-facing components are low fuel retention, as well as low erosion under high heat and particle fluxes. Tungsten (W) has been identified as a promising candidate<sup>1-3</sup> and is therefore presently used as plasma facing material in various devices such as in the ASDEX Upgrade (AUG) tokamak,<sup>4</sup> in the JET ITER-like wall<sup>5</sup> and in the ITER-like divertor in WEST.<sup>6</sup> Yet, strong line radiation of non-fully ionized tungsten at fusion relevant temperatures<sup>7</sup> can significantly cool the central plasma, deteriorating fusion performance. Consequently, central W accumulation has to be avoided to keep concentrations in the core plasma below  $10^{-5} - 10^{-4}$ .<sup>3,8</sup> In AUG, central wave heating is applied regularly for W impurity density control.<sup>9-11</sup> Yet, complete understanding of all W transport mechanisms involved is still an outstanding issue.

In present day devices, heavy impurity transport is dominated by neoclassical transport in the inner half radius.<sup>10-14</sup> Density peaking of the main ion species drives inward convection, whereas neoclassical temperature screening due to gradients of the main ion temperature gives rise to outward transport. However, poloidal asymmetries in the heavy impurity density distribution can enhance neoclassical transport of these species by up to an order of magnitude.<sup>12</sup> The large mass of high  $Z$  impurities causes localization on the low field side in rotating plasmas due to centrifugal forces, whereas the high charge leads to sensitivity of these impurities to variations in the background electrostatic potential, for example due to minority heating by ion cyclotron resonance heating (ICRH). Since the impact of poloidal asymmetries on neoclassical heavy impurity transport however is strongly dependent on collisionality and plasma gradients,<sup>12</sup> both central W accumulation<sup>15</sup> and enhanced outward W transport<sup>12</sup> can be observed due to poloidal asymmetries under different conditions.

The occurrence of saturated  $(m, n) = (1, 1)$  magnetohydrodynamic (MHD) modes observed regularly in AUG discharges heated by electron cyclotron resonance heating (ECRH) is occasionally suspected to facilitate outwards W transport<sup>11,16,17</sup> both directly through MHD transport of W and indirectly by modifying the background profiles, thus affecting neoclassical transport. Similarly, heavy impurity transport is enhanced by central wave heating.<sup>10,18</sup> Application of ECRH can lead to a suppression of the neoclassical pinch,<sup>16,19</sup> possibly in parts due to density profile flattening close to the magnetic axis.<sup>15</sup> Furthermore, greatly increased anomalous diffusive transport is observed with on-axis ECRH.<sup>10,19</sup> As the emergence of a saturated  $(1, 1)$  MHD mode is suspected to have a similar impact, the exact mechanism responsible for mitigation of central W accumulation under these conditions is not understood completely.

Since neoclassical contributions depend strongly on the main ion density and temperature profiles,<sup>12,13</sup> accurate modelling of main ion transport is a vital prerequisite to ultimately simulate trace W impurity transport. Towards this goal, the fast quasilinear gyrokinetic code QuaLiKiz<sup>20,21</sup> is coupled to the 1.5-dimensional transport code JETTO<sup>22,23</sup> and used for the first time for integrated modelling of an AUG discharge. Similar work has recently been carried out on JET.<sup>24</sup> QuaLiKiz calculates turbulent heat, particle and momentum fluxes driven by ion temperature gradient (ITG), trapped electron (TEM) and electron temperature gradient (ETG) modes. The computed quasilinear fluxes have been validated against nonlinear simulations (see Ref. 20 and references therein) and tested for predicting temperatures, densities and toroidal velocities in H mode pulses.<sup>21,25</sup> Thanks to recent numerical improvements,<sup>21</sup> QuaLiKiz can now be used routinely for time evolving predictions, modelling 1 s of plasma evolution in  $\sim 100$  CPUh.

In this work, trace W impurity transport simulations are performed for AUG H-mode discharge #31115 with primary heating by neutral beam injection (NBI), where a saturated (1, 1) MHD mode is observed in the presence of central, localized ECRH. As a prerequisite, predictive heat and particle simulations in the presence of light impurities are performed in the plasma core to validate the main ion transport mechanisms calculated against experimentally obtained temperature and density profiles for AUG discharge #31115. Since turbulent and neoclassical contributions to central transport are insufficient to describe experimental fluxes, the difference observed is prescribed additionally and attributed to MHD driven transport. Applying the steady-state profiles calculated in the presence or absence of central MHD transport, W impurity transport simulations are carried out to assess the importance of neoclassical and MHD driven transport in achieving a hollow W profile in AUG discharge #31115. Tungsten is treated in the trace limit, thus assuming no impact on main ion profiles in the simulations performed. However, impurity radiation from experimental measurements is taken into account evolving the latter profiles.

The rest of this paper is organized as follows. AUG discharge #31115 is described in Sec. 2. The setup of the predictive heat and particle transport simulations performed is summarized in Sec. 3, the results presented in Sec. 4. Important sensitivities of the density and temperature profiles calculated are discussed in Sec. 5. Simulations of trace W impurity transport are shown in Sec. 6. A summary and conclusion are given in Sec. 7. An overview of the JETTO-QuaLiKiz versions used for the simulations presented is provided in appendix A.

## 2 Description of ASDEX Upgrade discharge #31115

For the first time, integrated modelling of an ASDEX Upgrade plasma with the quasilinear gyrokinetic code QuaLiKiz is carried out. Discharge #31115 is chosen, since this particular shot is part of a dedicated W-transport study on avoidance of central W-accumulation, performed in early 2014. The effect of central MHD activity on W-behaviour is also discussed in Ref. 17 for the similar discharge #31114, part of the same experiment.

In discharge #31115 chosen for this study, H-mode confinement is achieved during the current flat top phase of 1 MA with an applied magnetic field of 2.5 T ( $q_{95} = 4.0$ ). The plasma is heated primarily by NBI with a base power of 7.3 MW (see time traces in Fig. 1(a)), delivered by two 93 kV beams and one 60 kV beam of equal power. An additional 60 kV beam is employed after around 2 s of H-mode at  $t = 3.5$  s, increasing the total NBI power to 9.7 MW. As fuelling is ensured by NBI, the flow of injected deuterium neutrals is simultaneously increased from  $8.5 \times 10^{20} \text{ s}^{-1}$  to  $12.0 \times 10^{20} \text{ s}^{-1}$ . Further heating of constant 1.4 MW is provided by electron cyclotron resonance heating (ECRH)<sup>26</sup> throughout the duration of the discharge with a narrow deposition profile close to the magnetic axis. Following the increase in NBI power, a transition in central MHD activity from sawteeth to a continuous  $(m, n) = (1, 1)$  mode is observed, as demonstrated by the on-axis electron temperature  $T_e(\rho_{\text{tor}} = 0)$ , measured by radiometry of electron cyclotron emission (ECE). Whereas a sudden drop in central  $T_e$ , followed by a gradual build-up, is captured periodically before  $t = 3.5$  s, the electron temperature response in the increased NBI-power phase is qualitatively different, oscillating with decreased frequency and amplitude (see Figs. 1(b), 2).

### 2.1 W-density response in phases of different MHD activity

In the discharge analysed, W-density profiles are derived from measurements by soft X-ray spectroscopy (SXR)<sup>17</sup> and by a grazing incidence spectrometer (GIW).<sup>17</sup> In the case of SXR,

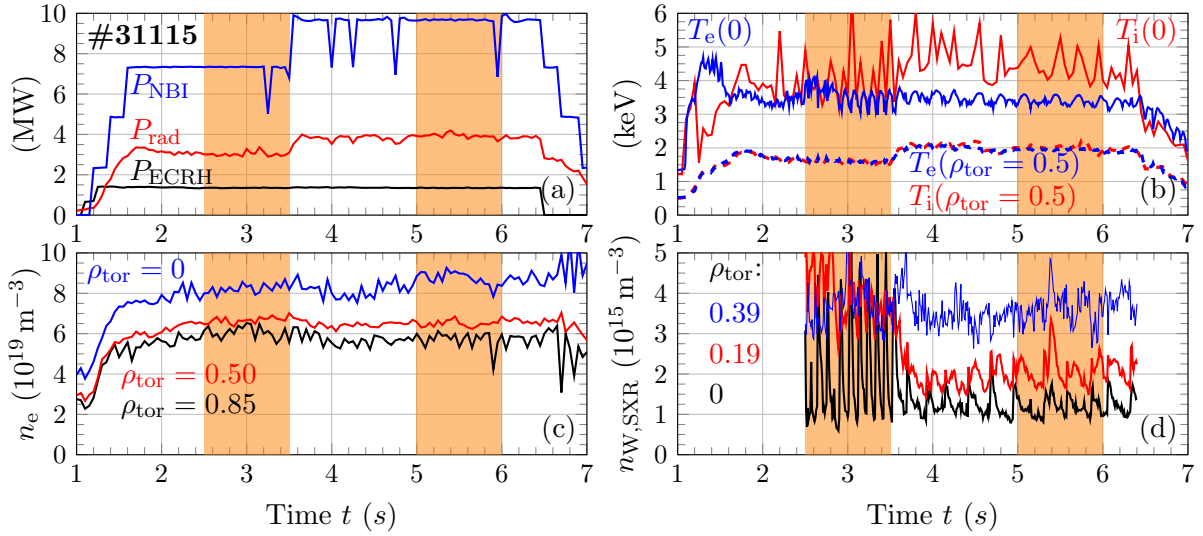


**Fig. 1:** Time traces of (a) the NBI, ECRH and radiated powers, (b) the species' temperatures  $T_s$  on axis and at mid-radius, (c) the electron density  $n_e$  on axis, at mid-radius and on top of the pedestal, and (d) the W-density  $n_{\text{W,SXR}}$  from X-ray spectroscopy (SXR) on-axis, at  $\rho_{\text{tor}} = 0.19$  and  $\rho_{\text{tor}} = 0.39$  for AUG discharge #31115. Shaded regions indicate the time slices used for predictive heat and particle transport simulations with JETTO and QuaLiKiz in this work.

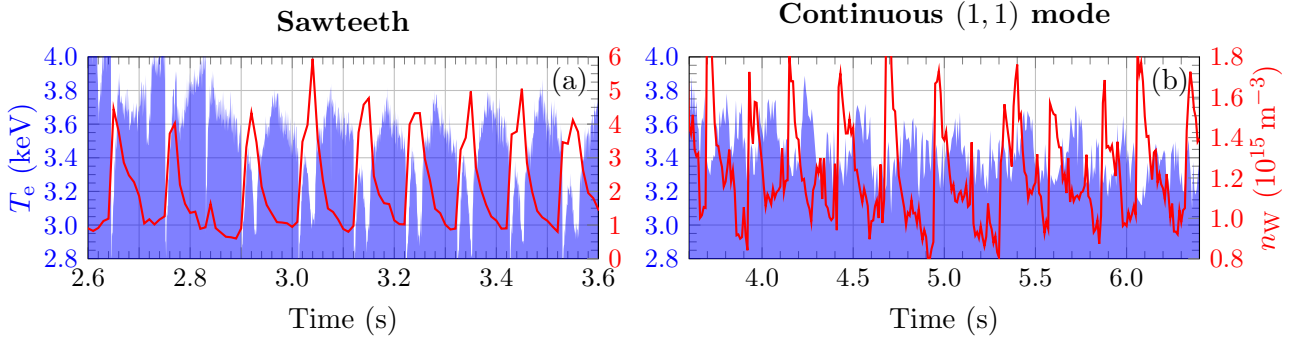


**Fig. 2:** On-axis electron temperature  $T_e$  (blue, left ordinate) and W-density  $n_{\text{W}}$  (red, right ordinate) for both phases of different NBI power, where either (a) sawteeth or (b) a continuous (1,1) mode is observed.

the local impurity density is obtained from Abel-inversion of the SXR emissivity from multiple line-of-sights, considering photons with energies exceeding 1 keV. Using the GIW diagnostic, the W-density is calculated from measurements of light with wavelengths around 5 nm from two different groups of W-ionization stages utilizing a single line-of-sight. Considering the fractional abundance profiles of the ionization stages involved, as well as electron temperature and density profiles, the local W-density in combination of shape and average position of each of the two emissivity measurements can be determined. A more general in depth description is given in Ref. 17, whereas the steps taken to obtain W-density profiles from raw measurements for this discharge are discussed in Ref. 16.

The behaviour of the on-axis W-density is qualitatively different in both phases of either sawteeth activity or in the presence of a continuous (1,1) mode, as inferred from the electron temperature response to these phenomena. In the first phase of the discharge, a deeply hollow W profile is observed (see Figs. 1(d), 3(a)), as is typically the case for ASDEX Upgrade discharges heated by ECRH,<sup>18</sup> with the W-density on axis being  $1.0 \times 10^{15} \text{ m}^{-3}$  and a maximum value of

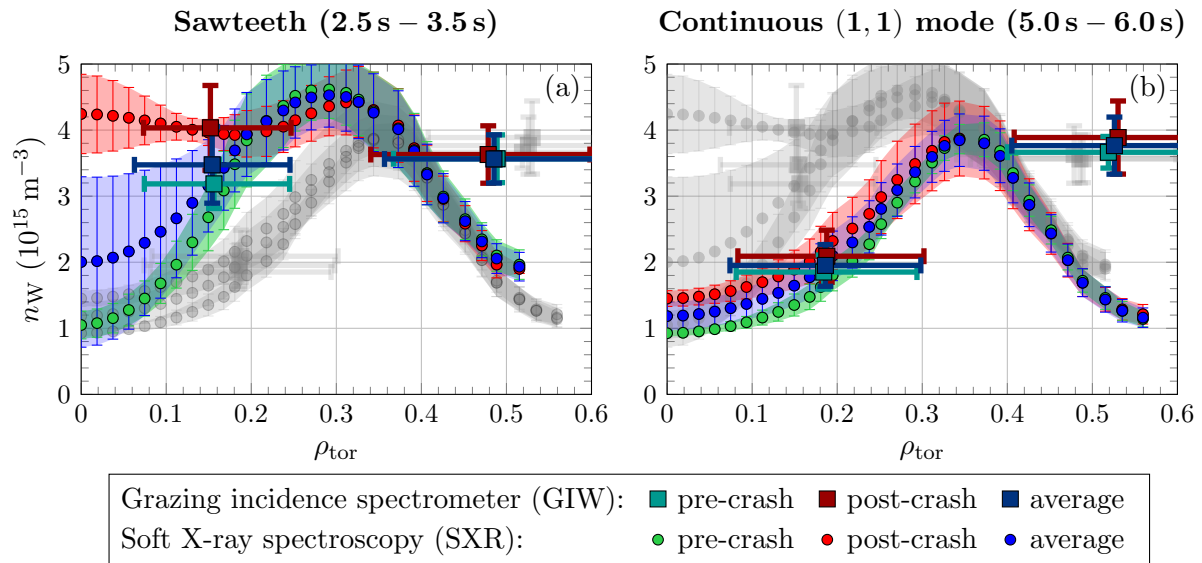


**Fig. 3:** Time-averaged W-density  $n_W$  in the presence of MHD activity, i.e. (a) sawteeth for  $t_1 \in [2.5 \text{ s}, 3.5 \text{ s}]$  and (b) a continuous (1, 1) mode for  $t_2 \in [5.0 \text{ s}, 6.0 \text{ s}]$ , as measured by a grazing incidence spectrometer (GIW) and soft X-ray spectroscopy (SXR). For each diagnostic, averaged minimum (green) and maximum density (red), i.e. in (a) the W-density prior to and just after the electron temperature crashes and in (b) the W-density during electron temperature maxima and minima, as well as the overall average density (blue) are shown. For comparison of the W-density response in phases of different MHD activity observed, W-density profiles illustrating MHD activity not present in a given phase of the discharge are depicted in light gray in the background of both graphs.

$4.6 \times 10^{15} \text{ m}^{-3}$  located at  $\rho_{\text{tor}} = 0.29$ . Measurements of core and peripheral GIW spectrometer yielding a core to mid-radius W-density ratio of 0.89 are in line with comparable discharges with central localized ECRH of 1.4 MW power (cf. Fig. 5 in Ref. 18).

The effect of sawteeth in the first phase of the discharge on the central W density is inverted with respect to the response of the electron temperature. While the latter exhibits periodically a sudden drop, the on-axis W-density increases simultaneously steeply to about  $4 \times 10^{15} \text{ m}^{-3}$  (see Figs. 2(a), 3(a)). In this process, the initially deeply hollow W-profile is flattened up to  $\rho_{\text{tor}} \simeq 0.4$ , affecting primarily the central W-density inside  $\rho_{\text{tor}} \simeq 0.2$ . Central W-accumulation is maintained for about 20 ms, followed by an exponential decay on similar temporal scales, thus re-establishing the hollow W-profile. With the onset of the net outward W-transport, the on-axis electron temperature builds up to its pre-crash value within a few ms. The W-response is in agreement with expected sawteething behaviour for a different initial condition than usually observed, in this case a hollow profile pre-crash, mixing the W-content up to the  $q = 1$ -surface, located at  $\rho_{\text{tor}} \simeq 0.4$ . Flattening of hollow W-profiles due to sawteeth has been reported in Ref. 16 for the preceding discharge #31114 and in Refs. 18, 27 for similar discharges.

In the presence of the continuous (1, 1) mode, the on-axis W-density fluctuates with decreased frequency and amplitude as compared to the sawteeth case (see Figs. 2, 3). As in the first part of the discharge, W-density fluctuations are of opposite phase as variations in the electron temperature. During minima of the central electron temperature, on-axis W-content is increased within a few ms from on average  $0.9 \times 10^{15} \text{ m}^{-3}$  to  $1.5 \times 10^{15} \text{ m}^{-3}$ , followed by an exponential decay to the initial value within 80-100 ms. Due to the small magnitude of the fluctuations, an overall deeply hollow W-profile is maintained throughout this process. As the maximum of the average density is both reduced to  $3.8 \times 10^{15} \text{ m}^{-3}$  and shifted outwards from

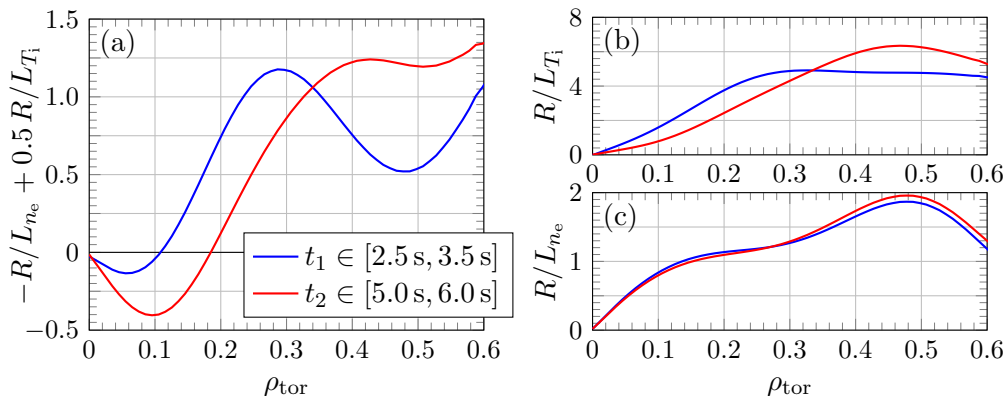


**Fig. 4:** Neoclassical pinch parameter  $-R/L_{n_i} + 0.5R/L_{T_i}$  (a), as well as normalized ion temperature gradient  $R/L_{T_i}$  (b) and normalized electron density gradient  $R/L_{n_e}$  (c) used to calculate the neoclassical pinch parameter in (a), averaged over time slices of 1s for both phases of different MHD activity, being the presence of sawtooth activity (blue) and of a continuous (1, 1) mode (red). Note that the normalized electron density gradient  $R/L_{n_e}$  was used as a surrogate for the normalized main ion density gradient  $R/L_{n_i}$ ; an approach valid for small values of  $Z_{\text{eff}}$ .

$\rho_{\text{tor}} = 0.29$  to  $0.34$ , the W-content in the inner half-radius is noticeably reduced during the presence of the continuous (1, 1) mode as compared to the first phase of the discharge. Hence in this case, the mechanism responsible is considerably more effective in establishing a hollow W-profile and thus in preventing central W-accumulation. Noticeably, W-density profiles observed during phases of different MHD activity agree within errorbars beyond  $\rho_{\text{tor}} \simeq 0.4$  for combined SXR and GIW measurements (see Fig. 3). Throughout the duration of the discharge, the  $q = 1$ -surface is calculated to be located similarly at  $\rho_{\text{tor}} \simeq 0.4$ , supporting the hypothesis that in the present case the continuous (1, 1) mode facilitates outward W-transport.<sup>16</sup>

To analyse the contributions of neoclassical transport to the evolution of the W-density profile, the analytical expression for the neoclassical convection to diffusion ratio is evaluated without taking poloidal asymmetries into account<sup>13</sup>

$$\frac{Rv_Z}{D_Z} = -Z \left[ \frac{R}{L_{n_i}} - \frac{1}{2} \frac{R}{L_{T_i}} \right]. \quad (1)$$

In the absence of a central W source, the normalized W-density gradient is directly determined by this ratio through  $R/L_{n_W} = -Rv_W/D_W$ . Note that this expression is valid for main ions in the banana and heavy trace impurities in the Pfirsch-Schlüter regime.<sup>13,28</sup> Deviating from either regime, the factor 1/2 in above equation is reduced.<sup>28</sup> Being for now only interested in a qualitative estimate, above expression is still suitable for a first analysis.

As illustrated in Fig. 4, expectations from neoclassical transport cannot explain the W-density response observed in either of the two phases of different MHD activity, as the average value of the neoclassical pinch parameter even suggests opposite behaviour<sup>1</sup>. In the first phase, W convection is directed outwards for  $\rho_{\text{tor}} \gtrsim 0.1$  due to the dominant effect of temperature screening over the neoclassical pinch. Increasing the NBI-power in the second phase of the discharge, the normalized electron density gradient  $R/L_{n_e}$  is unaffected by the simultaneous increase of

<sup>1</sup>Note, that these results are obtained substituting the normalized ion density gradient  $R/L_{n_i}$  with the normalized electron density gradient  $R/L_{n_e}$ . This is a reasonable approach for low values of  $Z_{\text{eff}}$ , which is here taken as  $Z_{\text{eff}} = 1.22$ .

NBI-fuelling, as the electron density response to the changing plasma operating conditions is negligible (see Figs. 4(c), 6(a,e,i,m)). However, a pronounced increase in the ion energy content is observed with increased beam power, generating steeper gradients at mid-radius and flattening the central profile (see Figs. 6(c,g,k,o)). As a result, the central normalized ion temperature gradient is reduced, weakening the effect of temperature screening and thus extending the region of inward W convection up to  $\rho_{\text{tor}} \simeq 0.2$ . Consequently an increase in W accumulation is expected, following this analytical consideration, in contrast to experimental observations. Although rotation induced poloidal asymmetries are not considered in above expression, their influence is expected to decrease the effect of temperature screening (cf. Refs. 12, 13) in both phases of the discharge due to similar levels of rotation (see Fig. 6(d,l)), hence increasing central inward W-convection in contrast to experimental observations. Temperature screening would be further reduced if trace W impurities were in the plateau regime instead of the Pfirsch-Schlüter regime, as assumed in Eq. (1). The possibility of MHD driven W transport thus arises.

## 2.2 Average plasma profile reconstruction

For quantitative comparison with predictive simulations, as well as for prescribing appropriate boundary conditions to the simulations, fits of the measured kinetic quantities are performed in both intervals simulated, being  $t_1 \in [2.5 \text{ s}, 3.5 \text{ s}]$  and  $t_2 \in [5.0 \text{ s}, 6.0 \text{ s}]$  (orange shaded regions in Fig. 1). The two intervals, covering 17.2 and 18.6 energy confinement times  $\tau_E$  respectively, are chosen to represent periods of comparatively stable plasma profiles within each phase. Merely one abnormal event in the evolution of the W-density is observed in the second interval at  $t = 5.39 \text{ s}$ , returning to usual levels within around 50 ms.

For both time slices considered, averaged plasma profiles are constructed from raw experimental data by applying Gaussian process regression techniques. A tool set created by A. Ho<sup>29</sup> was utilized, whose development was inspired by previous work carried out by M.A. Chilenski.<sup>30</sup> An overview of data used and profiles obtained is illustrated in Fig. 6. Electron density profiles are derived from combined core density measurements by Thomson scattering spectroscopy (TS) and edge density analysis by lithium beam spectroscopy (LIB). A relative radial inward shift of the TS-profiles of the order of 5 mm at the outer mid-plane is taken into account to compensate for estimated inaccuracies of the equilibrium and related mapping. In the case of the electron temperature, averaged profiles are calculated from ECE and TS data. Analysing charge exchange recombination spectroscopy (CXRS) measurements, both ion temperature and toroidal rotation velocity profiles are obtained. As the outermost channels of core CXRS consistently provide ion temperature measurements elevated with respect to spatially better resolved edge CXRS diagnostics, uncertainties of the core channels affected are increased artificially to decrease their weights during profile reconstruction. This discrepancy between CXRS diagnostics is occasionally observed in AUG due to, inter alia, insufficiently accurate NBI geometry and equilibrium applied during evaluation of core CXRS measurements, as well as due to intersections of the core diagnostic's line-of-sights with the edge pedestal (such that the assumption of constant impurity density along the LOS breaks down). A correction of the ion temperature mapping for these effects has been made available during finalization of this work and will be applied in future experiments.

The Gaussian process regression techniques applied utilize Bayesian probability theory under the assumption of normally distributed weights for profile reconstruction from covariance functions, referred to as kernels  $k(x, x')$ , thus ensuring a robust estimation of profiles, gradients and

associated uncertainties. Electron and ion temperature profiles are obtained using a rational quadratic kernel

$$k(x, x') = \sigma^2 \left[ 1 + \frac{(x - x')^2}{2\alpha l^2} \right]^{-\alpha}, \quad (2)$$

yielding smooth functions with characteristic length-scale  $l$ . This approach becomes inapplicable if a typically smooth target function is expected to change rapidly over a short distance, as is the case in the presence of transport barriers, necessitating a kernel with variable length-scale  $l(x)$ .<sup>29</sup>

$$\left. \begin{aligned} k(x, x') &= \sigma^2 \sqrt{\frac{2l(x)l(x')}{l^2(x) + l^2(x')}} \exp\left(-\frac{(x - x')^2}{l^2(x) + l^2(x')}\right), \\ l(x) &= l_0 - l_\mu \exp\left(-\frac{(x - \mu)^2}{2\sigma_\mu^2}\right) \end{aligned} \right\} \quad (3)$$

Given the reduced length-scale around  $x = \mu$ , pedestal behaviour is captured applying this covariance function to electron density and toroidal velocity data. Note that in either case, experimental measurements are weighted solely based on their uncertainties provided.

The overview of averaged raw experimental data and regression results illustrated in Fig. 6 showcases the capabilities of Gaussian process regression techniques to produce both profiles and associated uncertainties in agreement with observations without specification of a model describing expected behaviour.

### 3 Setup of predictive transport simulations

Predictive heat and particle transport simulations of ASDEX Upgrade shot #31115 are performed by JETTO in both phases of the discharge, evolving density and temperature profiles in time over the duration of 1 s, corresponding to around  $18 \tau_E$ , until steady-state profiles are obtained. Plasma profiles obtained by application of Gaussian process regression techniques to raw experimental data (see Sec. 2.2) are used as initial conditions for the simulations. Toroidal plasma rotation profiles available are taken into account for heat and particle transport predictions, yet are treated interpretively throughout the simulations. Particle deposition, auxiliary power deposition and radiative power loss profiles obtained from previous analysis with the TRANSP code<sup>31</sup> are used as sources and sinks in the respective particle and energy balance equations solved by JETTO. Within TRANSP, NBI power and particle deposition profiles are calculated by the Monte Carlo fast ion module NUBEAM.<sup>32</sup> Fluxes due to neoclassical phenomena are calculated by the code NCLASS,<sup>33</sup> turbulent fluxes due to ITG, TEM and ETG modes by QuaLiKiz, taking collisions and rotational effects ( $E \times B$  shearing) into account. Application of QuaLiKiz is restricted to the turbulence dominated region up to the pedestal top, i.e.  $\rho_{\text{tor}} \in [0.20, 0.85]$  (see Fig. 6). At smaller radial positions, turbulent contributions are negligible since turbulence is on the one hand often found stable (in these simulations usually up to  $\rho_{\text{tor}} \sim 0.3$ ) due to small normalized gradients, and on the other hand outweighed by MHD driven central transport. The presence of both steep gradients and additional MHD phenomena, in particular of ELMs, at locations exceeding  $\rho_{\text{tor}} = 0.85$  in this case necessitates application of additional ELM and edge transport barrier models (see e.g. Ref. 24). However,

as this study ultimately aims at core W-impurity transport modelling, density and temperature profile are treated interpretively in this particular plasma region. Additionally, L-mode Bohm turbulent transport<sup>34</sup> is included, where the constant numerical prefactors of the transport model are reduced to 10% to increase simulation robustness without noticeably affecting simulation results.

As the MHD activity observed is expected to set central profiles, the influence on central transport is mimicked by prescribing additional transport coefficients to the simulation inside the  $q = 1$  surface. Considering the averaged density and temperature profiles in the presence of sources and sinks described, the corresponding steady-state particle and energy balance equations are solved for the effective transport coefficients  $D_{\text{eff}}$  and  $\chi_{e/i,\text{eff}}$ . Performing predictive heat and particle transport simulations neglecting drive due to MHD activity, predicted transport coefficients  $D_{\text{pred}}$  and  $\chi_{e/i,\text{pred}}$  are obtained by summation over neoclassical and turbulent contributions

$$\left. \begin{aligned} D_{\text{pred}} &= \sum_{c \in \{\text{neo, turb}\}} \left[ D_c - v_c \frac{n_i}{\nabla_\rho n_i} \right] - v_{\text{ware}} \frac{n_i}{\nabla_\rho n_i}, \\ \chi_{e/i,\text{pred}} &= \sum_{c \in \{\text{neo, turb}\}} \chi_{e/i,c}. \end{aligned} \right\} \quad (4)$$

The difference in effective and predicted transport coefficients is assumed to be due to the effect of MHD activity not accounted for in the transport simulations carried out and is prescribed in following simulations. This approach ensures accurate description of central transport in the presence of phenomena not described by neoclassical or gyrokinetic theory, yielding an estimate for the contribution of MHD activity.

Plasma impurities are treated inside the impurity transport code SANCO,<sup>35</sup> assuming an average effective charge  $\langle Z_{\text{eff}} \rangle = 1.22$ , as derived from impurity density analysis by CXRS performed in the preceding discharge #31113,<sup>36</sup> where concentrations of 0.45 % B, 0.25 % C and 0.15 % N are observed. As these results are in line with assumptions made for the analysis of discharge #31114,<sup>16</sup> plasma conditions during shot #31115 (the subject of this study) can be expected comparable, justifying the use of the average effective charge  $\langle Z_{\text{eff}} \rangle$  specified. Moreover, estimates of the effective charge for this discharge of  $\langle Z_{\text{eff}} \rangle \gtrsim 1.8$  derived from Bremsstrahlung measurements are found incompatible with experimental profiles by predictive heat and particle transport simulations performed (see Sec. 5.2 for a sensitivity analysis of the simulation results on the impurity content), advocating the use of  $\langle Z_{\text{eff}} \rangle = 1.22$  throughout this study. The simulation results obtained are insensitive to the composition of low- $Z$  impurities throughout the simulation. Therefore, only C-impurities are considered, resembling most closely the average light impurity charge  $\langle Z_{\text{imp}} \rangle = 5.6$ .

The ion to electron temperature ratio boundary condition used throughout this study requires careful treatment considering raw experimental measurements, general behaviour of comparatively cold plasma observed in various machines and specifically in ASDEX Upgrade, as well as uncertainties of regression results. Applying Gaussian process regression techniques to raw temperature measurement, temperature ratio boundary conditions of  $T_i/T_e|_{bc} = 1.33$  and 1.42 are obtained in the first and second time slice respectively, corresponding to differences between electron and ion temperature of 200 – 300 eV (see Fig. 5). Under these conditions, severe density peaking is predicted by heat and particle transport simulations. However, as indicated

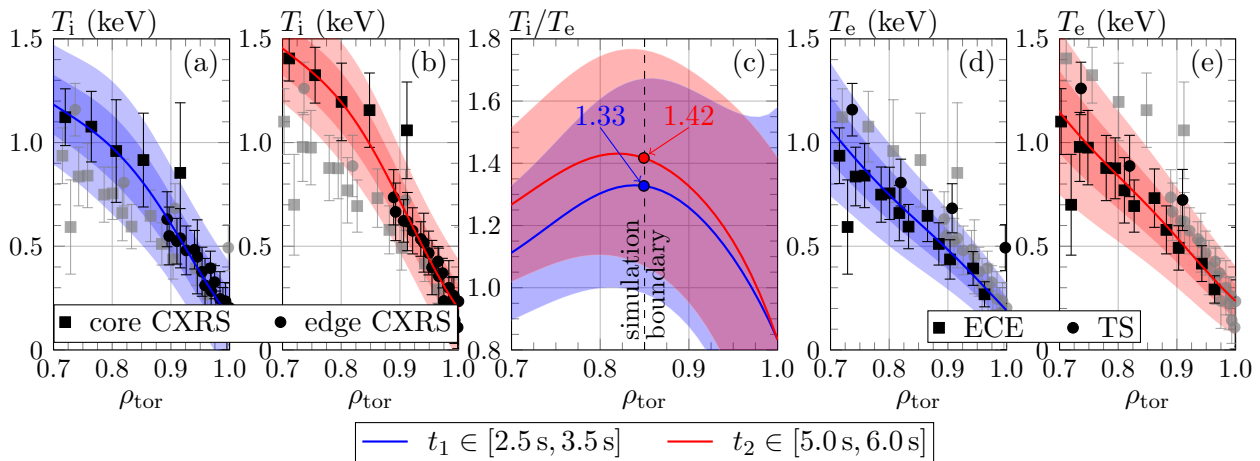


**Fig. 5:** Fits of the outer (a,b) ion temperature, (c) ion to electron temperature ratio and (d,e) electron temperature (solid lines) are obtained by applying Gaussian process regression techniques to raw data (black markers) from (a,b) core and edge charge exchange recombination spectroscopy (CXRS), as well as from (d,e) electron cyclotron emission (ECE) and Thomson scattering spectroscopy (TS). Temperature data corresponding to the time slices  $t_1 \in [2.5 \text{ s}, 3.5 \text{ s}]$  (blue) and  $t_2 \in [5.0 \text{ s}, 6.0 \text{ s}]$  (red) are depicted in (a,d) and (b,e) respectively, whereas the temperature ratio in (c) is shown for both time slices simultaneously. Shaded regions illustrate confidence intervals of  $1 \sigma$  (darker hue) and  $2 \sigma$  (lighter hue; not in (c)) of the regression results. For easier comparison of temperature measurements in a given time slice, electron and ion temperature data are additionally shown in light gray in the background of (a,b) and (d,e) respectively. Predictive heat and particle transport simulations are carried out inside  $\rho_{\text{tor}} = 0.85$ , treating temperature profiles for larger radii as fixed boundary conditions, thus preserving the temperature ratio at the simulation boundary.

by the significant uncertainties of  $T_i/T_e|_{\text{bc}}$ , the validity of the regression results is questionable when using raw CXRS measurements without further corrections, as supported by the following arguments.

In the case of ion temperature reconstruction, a discrepancy in temperature measurements of core and edge CXRS is observed in the pedestal region for this discharge. Estimates from the core diagnostics exceed the results from edge CXRS by  $300 - 400 \text{ eV}$  at  $\rho_{\text{tor}} = 0.90$ . However, measurements by the outer channels of core CXRS are likely subjected to mapping inaccuracies due to application of an insufficiently accurate NBI geometry and magnetic equilibrium during evaluation, and intersection of the LOS with the edge pedestal, thus reducing the confidence in the outermost channels of the core CXRS diagnostic. To decrease the weights during profile reconstruction, uncertainties of the corresponding channels of the core diagnostic are inflated to incorporate systemic uncertainties. However, as no reliable measurements in the vicinity of  $\rho_{\text{tor}} = 0.8$  are available, the regression procedure still noticeably emphasizes the core CXRS data, resulting in an elevated ion temperature profile in this region. Directly comparing ion temperature measurement from the edge CXRS diagnostic with electron temperature measurements by ECE and TS for  $\rho_{\text{tor}} \gtrsim 0.88$ , temperatures are found to agree within errorbars (see Fig. 5(d,e)). Noticeably, ion temperatures are estimated slightly larger than electron temperatures from ECE, yet estimated slightly lower than electron temperatures from TS. However, significant differences in temperature measurements are encountered in regions where the ion temperature is measured only by the core CXRS diagnostic. Consequently, it is reasonable to assume an overestimation of the ion temperature by the Gaussian process regression.

Simultaneously, electron temperature profiles obtained by regression can be assumed slightly

underestimated as a result of the difference in data density of both diagnostics incorporated. Measurements by ECE are consistently lower than estimates from TS, yet available at noticeably more radial locations beyond  $\rho_{\text{tor}} = 0.8$ . Consequently, the relative weights of the TS measurements are reduced in the regression procedure, resulting in the electron temperature profiles obtained to be influenced dominantly by estimates from ECE. As there are no reasons to question the validity of the measurements from each diagnostic, prioritization of one diagnostic over the other is unreasonable. Thus, the electron temperature profiles obtained by Gaussian process regression are assumed to be slightly underestimated.

Considering the high collisionality due to sub-keV particle temperatures in the vicinity of the simulation boundary, establishment of plasma conditions with temperature differences in the order of 200 – 300 eV is unlikely. Under typical experimental conditions, temperature ratios of  $T_i/T_e \sim 1.0$  are usually observed in the pedestal region across various machines,<sup>37,38</sup> as opposed to values of 1.33 and 1.42 obtained for this discharge.

Moreover, in AUG discharges heated both exclusively by NBI and by additional ECRH, ion-scale modes are usually unstable, according to turbulence diagnostics<sup>39,40</sup> and non-linear gyrokinetic simulations.<sup>40</sup> Yet, performing heat and particle transport simulations with JETTO and QuaLiKiz using the pedestal temperature profiles as suggested by Gaussian process regression, ITG modes are significantly stabilized in stationary conditions (see Sec. 5.1). The simultaneous destabilization of ETG modes necessitates increased net ion to electron heat transfer to satisfy the power balance. Consequently, electron heat transport constitutes the prime loss channel, with  $q_e/q_i|_{\text{bc}} = 4.2$  in the second time slice analysed<sup>2</sup>. This unobserved state predicted is imposed by the boundary condition, suggesting a reasonable modification of the pedestal temperature profiles used for predictive heat and particle transport simulations.

Given the uncertainties of the plasma profiles obtained with Gaussian process regression, temperature ratios with a confidence of  $1\sigma$  at the simulation boundary are found as  $1.33 \pm 0.34$  and  $1.42 \pm 0.35$  in each of the time slices analysed (see Fig. 5(c)). Following above discussion, a minor modification of the edge temperature profiles under consideration of their uncertainties is reasonable to approach experimental conditions. A more realistic temperature ratio boundary condition of  $T_i/T_e|_{\text{bc}} = 1.10$  is achieved in both time slices by symmetrically increasing the electron and decreasing the ion temperature at the simulation boundary by multiples of their respective uncertainty  $\sigma_{T_{e,i}}$  ( $t_1 : \pm 0.50 \sigma_{T_{e,i}}$ ,  $t_2 : \pm 0.75 \sigma_{T_{e,i}}$ ). This value of the ion to electron temperature ratio boundary condition is used throughout the rest of this study.

Performing predictive heat and particle transport simulations as described using 51 grid points, the temporal evolution of 1 s of ASDEX Upgrade plasma is calculated by JETTO-SANCO and QuaLiKiz within 5 - 9 h on 16 CPUs. As the simulation of a single time step with a maximum step size of 1 ms takes on average 16 s, total computation time is determined primarily by the number of time steps needed.

## 4 Predictive heat and particle transport simulations

### 4.1 Successful modelling by JETTO and QuaLiKiz

Heat and particle transport of ASDEX Upgrade discharge #31115 are predicted successfully by JETTO-QuaLiKiz, demonstrating good agreement with the experimental average at all radial positions inside the boundary condition at  $\rho_{\text{tor}} = 0.85$  for both time slices analysed. A

<sup>2</sup>Electron and ion heat fluxes  $q_s$  considering auxiliary NBI and ECRH heating, ion to electron heat transfer and radiative losses.

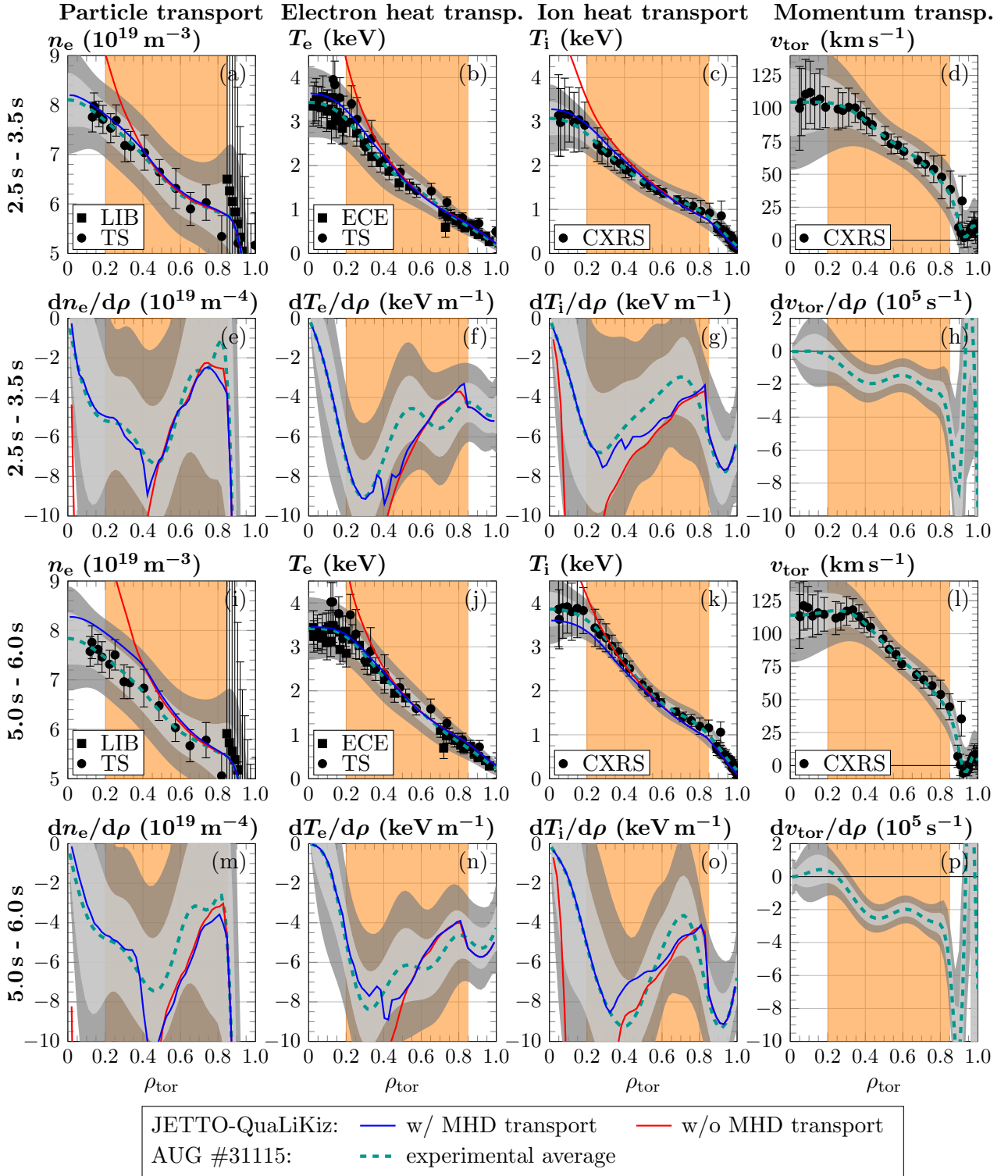


**Fig. 6:** Predictive particle and heat transport simulations performed by JETTO-QuaLiKiz for both time slices  $t_1 \in [2.5 \text{ s}, 3.5 \text{ s}]$  and  $t_2 \in [5.0 \text{ s}, 6.0 \text{ s}]$  analysed, with additional transport due to MHD effects included (solid blue) or omitted (solid red), compared to the averaged plasma profiles (dashed green) with confidence intervals of  $1\sigma$  and  $2\sigma$  (grey) for both time slices. Turbulent fluxes are calculated by QuaLiKiz in the region  $\rho_{\text{tor}} \in [0.20, 0.85]$ , corresponding to the orange shaded domain. Plasma profiles are obtained by Gaussian process regression using averaged raw experimental data (black markers). (a,e,i,m) Averaged electron density profiles  $n_e$  are obtained from lithium beam emission spectroscopy (LIB) and Thomson scattering spectroscopy (TS), (b,f,j,n) averaged electron temperature profiles  $T_e$  from electron cyclotron emission (ECE) and TS, and (c,g,k,o) averaged ion temperature  $T_i$  as well as (d,h,l,p) averaged toroidal velocity profiles  $v_{\text{tor}}$  from charge exchange recombination spectroscopy (CXRS).

**Table 1:** Agreement of density and temperature profiles, as well as of associated gradients, calculated in predictive particle and heat transport simulations with the experimental average in both time slices  $t_1 \in [2.5\text{ s}, 3.5\text{ s}]$  and  $t_2 \in [5.0\text{ s}, 6.0\text{ s}]$ . Average, maximum and on-axis deviation are expressed with respect to both the absolute value (%) and the standard deviation ( $\sigma$ ) of the experimental average. Average deviations are taken inside the region  $\rho_{\text{tor}} \in [0.20, 0.85]$  where QuaLiKiz is applied.

		Average deviation		Maximum deviation		On-axis deviation	
		(%)	( $\sigma$ )	(%)	( $\sigma$ )	(%)	( $\sigma$ )
Electron density $n_e$ :	$t_1$	$1.2 \pm 0.5$	$0.20 \pm 0.10$	1.8	0.35	1.2	0.18
	$t_2$	$4.7 \pm 2.6$	$0.76 \pm 0.48$	7.8	1.29	5.6	0.83
Gradient $dn_e/d\rho$ :	$t_1$	$19.4 \pm 40.3$	$0.14 \pm 0.13$	209.1	0.56		
	$t_2$	$31.0 \pm 22.6$	$0.46 \pm 0.37$	80.5	1.17		
Electron temperature $T_e$ :	$t_1$	$5.3 \pm 2.8$	$0.40 \pm 0.23$	9.8	0.73	5.9	0.51
	$t_2$	$3.7 \pm 3.3$	$0.25 \pm 0.18$	13.7	0.71	1.0	0.09
Gradient $dT_e/d\rho$ :	$t_1$	$20.0 \pm 16.5$	$0.69 \pm 0.53$	51.1	1.63		
	$t_2$	$13.8 \pm 6.1$	$0.53 \pm 0.22$	25.2	1.07		
Ion temperature $T_i$ :	$t_1$	$7.0 \pm 3.0$	$0.71 \pm 0.32$	11.7	1.08	6.9	0.55
	$t_2$	$7.5 \pm 2.9$	$1.02 \pm 0.31$	13.3	1.53	6.7	0.65
Gradient $dT_i/d\rho$ :	$t_1$	$23.2 \pm 15.9$	$0.50 \pm 0.33$	55.4	1.12		
	$t_2$	$14.5 \pm 10.7$	$0.45 \pm 0.36$	36.1	1.39		

comparison of calculated density and temperature profiles against the experimental averages is depicted in Fig. 6. All plasma profiles obtained agree within 14% with the absolute value of the experimental average, whereas the average deviation of a single modelled profile is within 8%. In terms of the standard deviation  $\sigma$  of the experimental average obtained by Gaussian process regression, predicted density and temperature profiles agree within  $1.6\sigma$ , with the average deviation of a single predicted profile being below  $1.0\sigma$ , showing overall good agreement of simulation and experiment. A more detailed overview of average, maximum and on-axis deviation for each of the three profiles predicted and associated gradients is presented in Table 1.

Reproducing experimental gradients, predictions are found to agree usually within 50%. However, the largest deviations are observed in the vicinity of the boundary condition around  $\rho_{\text{tor}} \sim 0.8$  where experimental profiles are comparatively flat due to the presence of a density pedestal. Hence, minor deviations in gradient predictions result in large relative disagreement. Taking the agreement of all radial points between  $\rho_{\text{tor}} = 0.2$  and the boundary condition into consideration, i.e. in the domain where QuaLiKiz is applied for the calculation of turbulent fluxes, individual gradients are on average predicted typically within around 20% of the experimental gradients, corresponding to average deviations of less than  $0.7\sigma$ . Consequently, heat and main ion transport in ASDEX Upgrade discharge #31115 are found to be modelled correctly by JETTO-QuaLiKiz within uncertainties.

Closer analysing the simulation results, agreement in turbulence driven transport predicted by QuaLiKiz outside  $\rho_{\text{tor}} \sim 0.4$  determines central profile agreement. Inside the  $q = 1$  surface, plasma gradients are described typically exact as a result of the imposed transport matching. Consequently, deviations of the calculated gradients inside the turbulence dominated region propagate into the central plasma through integration, thus determining central profile agreement. As the gradients predicted describe the experimental situation well, generally good central agreement is observed for all profiles calculated (see Fig. 6).

Particularly good agreement is achieved for particle transport in the first phase of the discharge, as well as for electron heat transport in the second time slice, where on-axis deviations of only 1.2% and 1.0% respectively are observed (see Table 1). Moreover, particle transport in the first phase is predicted with very good agreement with experimental observations for all radial positions, exhibiting only minor deviations in the electron density profile and the corresponding gradient. A similar degree of agreement is achieved calculating the electron temperature profile in the second time slice. Even though the exact shape of the respective gradient is not reproduced, the general trend is captured on average, cancelling out local deviations in transport predictions from observations, thus yielding agreement in predicted electron temperature profile and experimental average.

Predicted gradients of both phases of the discharge show agreement in a number of parameters in the turbulence dominated region. Considering particle transport, the average slope of both density gradients is similar for both phases of the discharges. However, whereas very good agreement with the experimental average is achieved in the first phase of the discharge, the electron density gradient obtained in the region  $\rho_{\text{tor}} \in [0.45, 0.75]$  in the second time slice is on-average steeper by  $(2.3 \pm 0.5) \times 10^{19} \text{ m}^{-4}$  as compared to the gradient predicted in the previous phase (see Figs. 6(d,j)). As the experimental gradients do not change significantly between phases of different NBI power and fuelling, decreased agreement between simulation and experiment is observed in the second phase of the discharge. Nevertheless, even though turbulent transport is noticeably underestimated, the calculated density profile still describes the experimental average well, with deviations being below 8%.

Comparing electron heat transport simulations for both time slices analysed, predicted gradients in the region  $\rho_{\text{tor}} \in [0.4, 0.8]$  agree on average within  $(4 \pm 3)\%$  with each other, being virtually unaffected by an increase in NBI power, NBI fuelling and changing boundary conditions between time slices (see Figs. 6(e,k)). Consequently, the difference observed in predicted electron temperature profiles is determined by the electron temperature boundary condition. Analysing the electron temperature profile measured experimentally in both phases of the discharge, a peaked temperature profile is observed in the first phase, corresponding to steep gradients around  $\rho_{\text{tor}} \sim 0.3$  and on-average constant gradients in the outer half-radius. Entering the second phase of the discharge, on-axis electron temperature remains constant, whereas the central profile is broadened due to increased NBI heating and net ion-to-electron heat exchange, reducing central temperature peaking and increasing temperature gradients in the turbulence dominated region. Consequently, temperature gradients are observed to change on-average linearly with the radial coordinate  $\rho_{\text{tor}}$  in the second time slice. Under these conditions, excellent agreement between simulation and experiment is achieved, as the gradients calculated by JETTO-QuaLiKiz are generally found to increase linearly with  $\rho_{\text{tor}}$  in the turbulence dominated region. However, the situation of a peaked central profile characterized by an approximately constant gradient in the outer half-radius in the first time slice is described with a reduced degree of agreement, as JETTO-QuaLiKiz captures the shape of the temperature gradient with less success. Still, even in this case, only small deviations below 10% are observed, illustrating overall successful electron heat transport simulations.

Considering ion heat transport, an increase in the ion temperature gradient is predicted in the turbulence dominated region during the second phase of the discharge as compared to the first time slice (see Figs. 6(f,l)), capturing the measured gradient on-average and thus the overall increase of ion temperature due to additional NBI heating. However, as the ion temperature

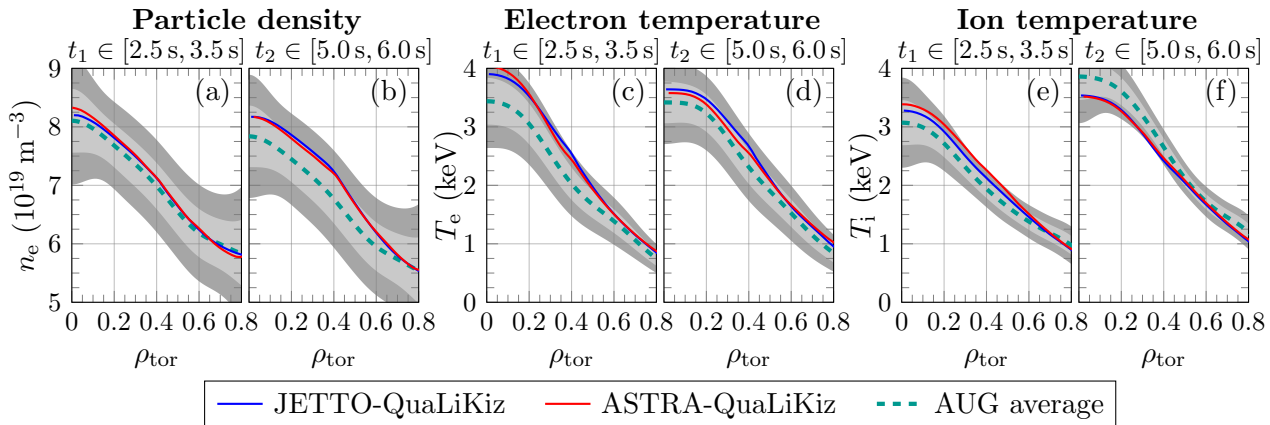


**Fig. 7:** Predictive heat and particle transport simulations performed by JETTO-QuaLiKiz (blue) and ASTRA-QuaLiKiz (red) showing (a,b) electron density, (c,d) electron temperature and (e,f) ion temperature profiles compared to the experimental average of AUG #31115 (dashed green) with confidence intervals of  $1\sigma$  and  $2\sigma$  (grey) in both time slices  $t_1 \in [2.5\text{ s}, 3.5\text{ s}]$  and  $t_2 \in [5.0\text{ s}, 6.0\text{ s}]$ . Note, that the benchmark was carried out with an updated version of JETTO-QuaLiKiz (see appendix A).

at the simulation boundary is reduced to provide a more reasonable temperature ratio  $T_i/T_e|_{bc}$  (see Sec. 5.1 for a discussion on the influence of  $T_i/T_e|_{bc}$  on the agreement between simulation and experiment), the ion temperature profile in the second time slice is slightly underestimated, yet still agreeing within 14% with the experimental average.

It should be emphasized, that the experimental average of the profiles obtained by JETTO and QuaLiKiz are compared against is the result of Gaussian process regression and is thus subjected to uncertainties. Consequently, assessing the capability of JETTO-QuaLiKiz to reproduce ASDEX Upgrade discharges, both uncertainties obtained from regression as well as from raw experimental data directly are to be taken into account. As simulation results are found to agree well within regression uncertainties, even for the cases of least agreement, and confidently represent raw experimental data, JETTO-QuaLiKiz are found capable of simulating ASDEX Upgrade discharges within errorbars.

## 4.2 Comparison of transport predictions between ASTRA and JETTO

To ensure a consistent implementation of QuaLiKiz in standard transport codes, the predictive heat and particle transport simulations performed by JETTO-QuaLiKiz for AUG #31115 are repeated exchanging the transport code JETTO for the Automated System for TRansport Analysis (ASTRA).<sup>41,42</sup> For this purpose, a modified version of JETTO-QuaLiKiz is used to ensure identical treatment of the radial electric field in both ASTRA and JETTO (see appendix A). Calculations with ASTRA-QuaLiKiz are carried out for both time slices evolving the steady-state solutions obtained with JETTO-QuaLiKiz until plasma profiles are converged. Since steady-state profiles are calculated usually independently of the initial conditions prescribed, this approach is expected to yield almost identical steady-state solutions as simulations performed utilizing the experimental averaged plasma profiles initially.

The steady-state density and temperature profiles obtained by ASTRA-QuaLiKiz are in good agreement with predictions by JETTO-QuaLiKiz in both time slices analysed (see Fig. 7). Both on-axis deviations and average deviations in the turbulence between plasma profiles predicted by both implementations are within 4%. Similarly, good agreement is observed in the corresponding transport coefficients calculated by QuaLiKiz inside both transport codes. Consequently,

deviations in predicted gradients are small as well, resulting in the excellent agreement of calculated plasma profiles. Even though agreement is not strictly exact for any of the transport channels, the minor differences observed may not necessarily point towards a difference in implementation of QuaLiKiz between both transport codes. Small differences in predicted plasma profiles may result from a different treatment of the magnetic geometry, from a difference in numerical schemes utilized or from applying different smoothing methods to the transport coefficients obtained.

### 4.3 Influence of MHD induced transport on central profile agreement

Agreement in particle and heat transport inside the  $q = 1$  surface at  $\rho_{\text{tor}} \sim 0.4$  is obtained only when prescribing additional transport coefficients to mimic the effect of central MHD activity (see Fig. 6). When omitting this contribution, central transport is found significantly reduced, requiring predictive simulations over a prolonged duration, as steady state is not reached after evolving the plasma profiles over 1 s. However, as the simulations omitting additional transport are qualitative only, profiles obtained after 1 s of temporal evolution are showcased. To demonstrate the absence of central turbulence transport, QuaLiKiz is applied down to the magnetic axis, as opposed to the simulations including additional transport coefficients, where turbulent contributions are obtained only down to  $\rho_{\text{tor}} = 0.2$ .

#### 4.3.1 Transport simulations excluding additional central transport

Omitting transport coefficients due to MHD activity (see Fig. 6), particle transport simulations predict on-axis densities increased by as much as 80% in both time slices analysed ( $t_1$ :  $+3.3 \times 10^{19} \text{ m}^{-3}$ ,  $t_2$ :  $+6.0 \times 10^{19} \text{ m}^{-3}$ ). Similarly, heat transport predictions put the on-axis electron temperature at just below 15 keV, corresponding to an increase of more than 11 keV, and overestimate central ion temperature by 1.8 keV. As the additional transport coefficients are prescribed inside  $\rho_{\text{tor}} = 0.4$  only, plasma profiles beyond are predicted identical in both cases under consideration of numerical phenomena. The same holds for normalized plasma gradients, being significantly overestimated inside  $\rho_{\text{tor}} \sim 0.4$  in the absence of additional central transport. A comparison of normalized gradients for both cases is illustrated in Fig. 8 for the first time slice analysed only, as the situation is similar in both phases of the discharge. As additional transport is included to obtain central transport agreement, normalized gradients in this case are close to the experimental profiles. Hence, normalized gradients are severely overestimated in the absence of enhanced central transport coefficients, as shown in Figs. 6 and 8.

Note, that all gradients shown in Fig. 8 are obtained by averaging the last 0.5 s of the simulation. The finite standard deviation of gradients inside the  $q = 1$  surface in the absence of additional central transport illustrates that simulated plasma profiles are still in the process of converging in the second half of the simulation, whereas a steady state central solution is already obtained including enhanced transport coefficients, demonstrated by the vanishing standard deviation in this case. Similarly, an equilibrium is reached beyond  $\rho_{\text{tor}} \sim 0.4$ .

In the case of particle transport, omitting the effect of MHD, normalized gradients inside the  $q = 1$  surface are as high as  $R/L_{n_e} = 4$ , as compared to values ranging between  $R/L_{n_e} \sim 1-2$  in the turbulence dominated region. Similarly, central normalized electron temperature gradients are found being as large as  $R/L_{T_e} = 20$ , constituting a significant increase from the average value of  $R/L_{T_e} \sim 7$  present in the turbulence dominated region. Central normalized ion temperature gradients remain at the level of the turbulence dominated regime down to  $\rho_{\text{tor}} \sim 0.1$ , being

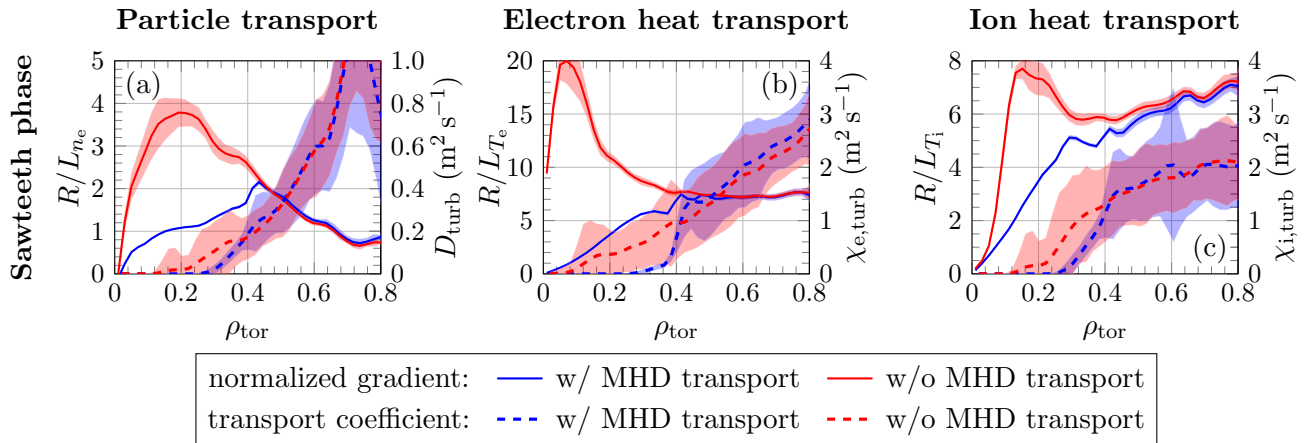


**Fig. 8:** (a) Particle, (b) electron heat and (c) ion heat transport from predictive simulations with JETTO-QuaLiKiz in the presence (blue) or in the absence (red) of additional transport coefficients inside  $\rho_{tor} = 0.4$ , mimicking the effect of MHD activity. Associated normalized gradients (solid, left ordinate), as well as the turbulent transport coefficients  $D_{turb}$  and  $\chi_{turb}$  calculated by QuaLiKiz (dashed, right ordinate) are averaged over the last 0.5 s of the simulations of the first time slice. Note, that the transport coefficients shown do not include contributions due to MHD activity or neoclassical phenomena. The shaded regions represent the standard deviations of the quantities presented, demonstrating the non-stationary behaviour of the normalized plasma gradients in the last 0.5 s of plasma evolution when omitting MHD transport.

$R/L_{Ti} \sim 6 - 8$ . However in the presence of additional central transport, normalized gradients change approximately linearly between magnetic axis and  $q = 1$  surface. On a side note, as normalized density gradients observed in this discharge are comparatively low (see Fig. 8(a)), ion scale turbulence is found to be determined by ITG modes. Hence, critical density gradients for TEM destabilization are not reached.<sup>43,44</sup>

Including additional central transport, turbulence is stabilized inside  $\rho_{tor} \sim 0.3$ . Here, barely any unstable modes are present, as indicated by turbulent particle and heat transport coefficients, since normalized gradients are decreased below their critical values by enhanced central transport. Turbulent transport coefficients presented in Fig. 8 for the first time slice analysed are averaged over the last 0.5 s of plasma evolution, highlighting the reduced turbulence levels inside  $\rho_{tor} \sim 0.4$ , as standard deviations of the averaged transport coefficients are negligible. Neglecting the effect of central MHD, neoclassical transport is insufficient in maintaining central plasma profiles, even though neoclassical transport increases with respect to case considering MHD influence for all transport channels. Gradients increase up to their critical value where turbulence is driven unstable, thus setting central profiles. Correspondingly, finite turbulent transport coefficients are observed down to  $\rho_{tor} \sim 0.1$ , although decreased as compared to the amplitude found in the turbulence dominated region, as steep normalized gradients are present in the plasma centre. Hence, additional transport coefficients describing the influence of central MHD activity are vital to obtain agreement in central transport.

#### 4.3.2 Magnitude of MHD induced central transport

The transport coefficients prescribed for both phases of the discharge are illustrated in Fig. 9. In the vicinity of the  $q = 1$  surface, the additional particle diffusivity prescribed is between 0.1 and  $0.3 m^2 s^{-1}$ , whereas additional heat transport is roughly around  $1 m^2 s^{-1}$ . Compared to contributions from turbulent transport in the same region, transport coefficients due to MHD

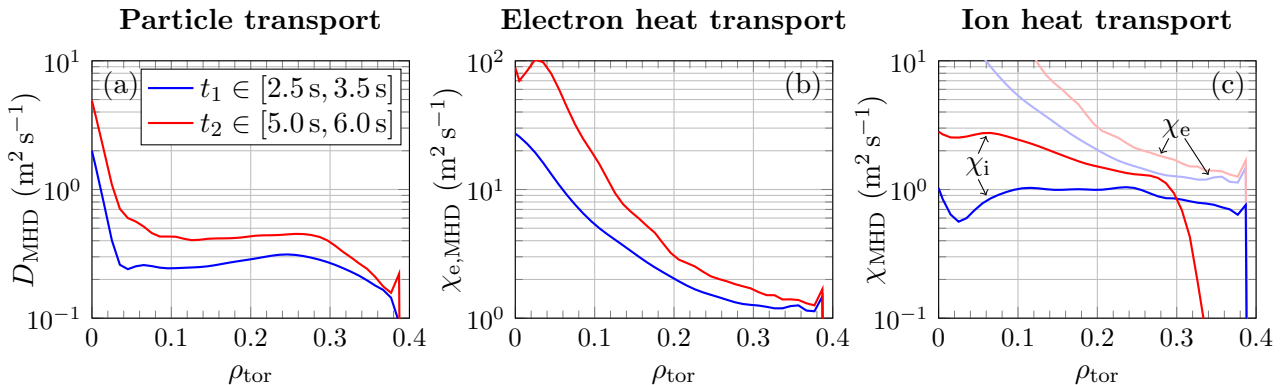


**Fig. 9:** Additional (a) particle, (b) electron heat and (c) ion heat transport coefficients prescribed in predictive transport simulations to mimic the effect of MHD activity inside the  $q = 1$  surface, being sawteeth in time slice  $t_1 \in [2.5 \text{ s}, 3.5 \text{ s}]$  (blue) and a continuous (1, 1) mode in time slice  $t_2 \in [5.0 \text{ s}, 6.0 \text{ s}]$  (red). In (c), electron heat transport coefficients are additionally shown in pale colors to allow for easier comparison with ion heat transport coefficients (bold colors).

activity for all three channels are of similar amplitude (cf. Fig. 8). In the case of particle and ion heat transport, additional coefficients prescribed are usually approximately constant inside  $\rho_{\text{tor}} \sim 0.3$  at a level slightly elevated as compared to the value at the  $q = 1$  surface. On the magnetic axis, strongly enhanced particle and electron heat transport is observed.

In the presence of the continuous (1, 1) MHD mode, additional transport coefficients necessary to obtain transport agreement inside the  $q = 1$  surface are noticeably larger for all transport channels as compared to the phase where sawteeth are observed. Differences are most dominant on the magnetic axis, where transport driven by the continuous (1, 1) mode is larger by a factor of 2.5 – 3.3. Approaching the  $q = 1$  surface, comparable levels of transport are encountered for both phenomena. Overall, the additional transport coefficients prescribed demonstrate increased outward transport due to the effect of the continuous (1, 1) MHD mode.

The additional transport coefficients prescribed are prone to errors due to uncertainties in the input profiles of the respective balance equations, i.e. particle and power deposition profiles as well as average plasma profiles. Vanishing on-axis gradients demand comparatively large transport coefficients to match heat and particle fluxes deposited. As the relative uncertainties in the gradients obtained are quite large (see Figs. 6), confidence in the calculated effective transport coefficients close to the magnetic axis is reduced. Additionally in the case of electron heat transport, the footprint of the ECRH power deposition profile is imprinted in the effective heat diffusivity, as the entire 1.4 MW of auxiliary power are deposited within  $\rho_{\text{tor}} = 0.2$ , demanding a large heat conductivity to ensure energy balance. Since turbulent and neoclassical contributions to both ion and electron heat transport are negligible inside  $\rho_{\text{tor}} = 0.2$ , MHD driven heat transport coefficients are determined primarily by the effective transport coefficients and associated uncertainties. In the case of particle transport, considerable contributions from inward pinches and neoclassical phenomena reduce the influence of the effective particle diffusivity in calculating the MHD contribution, yet introduce further uncertainties.

Considering the effect of the additional particle diffusivity prescribed on central W-transport under the assumption of identical transport coefficients for electrons and W, the increase in diffusivity observed between both phases of the discharge is in alignment with the experimental observation, that central W-accumulation is noticeably reduced with the onset of the continuous (1, 1) mode. This suggests that the mechanism present in the second phase of the discharge

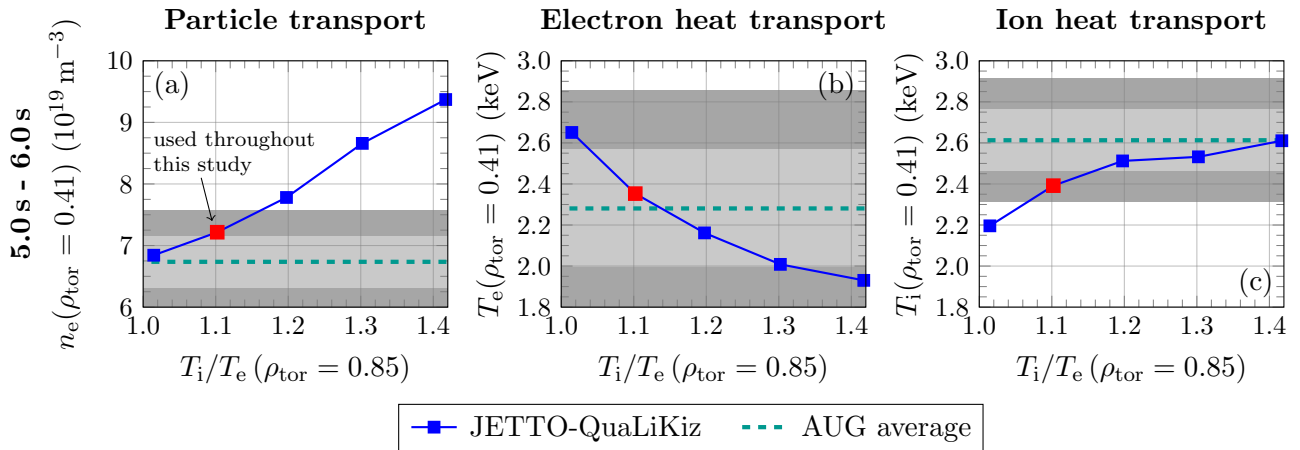


**Fig. 10:** Plasma response at  $\rho_{\text{tor}} = 0.41$  to the  $T_i/T_e|_{\text{bc}}$  boundary condition for the time slice  $t_2 \in [5.0 \text{ s}, 6.0 \text{ s}]$ . From the temperature profiles obtained by Gaussian process regression ( $T_i/T_e|_{\text{bc}} = 1.42$ ), different ratios  $T_i/T_e|_{\text{bc}}$  are obtained by increasing  $T_e$  and reducing  $T_i$  symmetrically by multiples of their respective standard deviations  $\sigma_{T_s}$  at the pedestal. The value  $T_i/T_e|_{\text{bc}} = 1.10$  used for predictive heat and particle transport simulations throughout the rest of this study is emphasized by a red square. Predicted (a) electron density, (b) electron temperature and (c) ion temperature (solid blue) compared to the averaged plasma profile (dashed green) with confidence intervals of  $1\sigma$  and  $2\sigma$  (grey). The behaviour illustrated is qualitatively observed at all radial positions.

is more efficient. Since a difference between both phases is the presence of a continuous  $(1, 1)$  mode in the latter, this particular mode might perhaps indeed facilitate outward W transport.

## 5 Simulation sensitivity on plasma parameters

Throughout the preparation of this study, plasma profiles calculated in predictive heat and particle transport simulations by JETTO-QuaLiKiz were found sensitive to a reasonable variation of various plasma parameters. The dependence of density and temperature profile predictions on the following quantities is discussed in the upcoming sections: dependence on the ion to electron temperature ratio  $T_i/T_e|_{\text{bc}}$  prescribed at the boundary condition (Sec. 5.1), influence of the average effective charge  $\langle Z_{\text{eff}} \rangle$  (Sec. 5.2), effect of the NBI particle source assumed (Sec. 5.3), impact of reduced collisionality (Sec. 5.4).

### 5.1 Influence of the ion to electron temperature boundary condition on core transport

The predictive heat and particle transport simulations performed are found sensitive to the imposed ion to electron temperature  $T_i/T_e|_{\text{bc}}$  boundary condition at  $\rho_{\text{tor}} = 0.85$ . For values of  $T_i/T_e|_{\text{bc}}$  exceeding 1.2, severe density peaking is observed throughout the core plasma whereas heat transport is less affected by a variation in  $T_i/T_e|_{\text{bc}}$  (see Fig. 10). A detailed description of the effects of an elevated temperature ratio boundary condition on the simulation results is given in Sec. 5.1.1. A physical interpretation of the phenomena observed is presented in Sec. 5.1.2. Even though this effect is present in both time slices considered, the discussion will be limited to time slice  $t_2 \in [5.0 \text{ s}, 6.0 \text{ s}]$ .

#### 5.1.1 Observations from predictive transport simulations

Performing simulations evolving the initial profiles obtained with Gaussian process regression from experimental measurements, the ion to electron temperature boundary condition is prescribed as  $T_i/T_e|_{\text{bc}} = 1.42$ . Under these conditions, the electron density is overestimated on-axis

by  $2.8 \times 10^{19} \text{ m}^{-3}$ , corresponding to 36% of the central experimental average (cf. Fig. 10(a)<sup>3</sup>). However since plasma profiles are treated interpretively beyond  $\rho_{\text{tor}} = 0.85$ , electron density profile evolution is modelled only on top of the H-mode pedestal. Expressed in terms of the increase between pedestal shoulder and magnetic axis, the central density is overpredicted by more than 110%. Approaching a temperature ratio of unity at the simulation boundary, agreement of the predicted on-axis electron density with the experimental average is improved significantly to within 4%. Starting from the temperature profiles obtained through regression, different temperature ratio boundary conditions are constructed by simultaneously increasing the electron and decreasing the ion temperature in the respective domain of the plasma by up to one standard deviation.

Regarding heat transport, on-axis temperatures are underestimated by up to 16% using the Gaussian process regression results of  $T_i/T_e|_{\text{bc}} = 1.42$ , thus being less affected than particle transport calculations by a temperature ratio boundary condition significantly exceeding unity. However, the electron temperature response to a reduction of  $T_i/T_e|_{\text{bc}}$  is qualitatively different, exhibiting increased temperature peaking as the temperature ratio boundary condition is reduced to unity (see Fig. 10(b)). Still, in the predictive heat transport simulation performed, central electron temperatures agree within  $2\sigma$  with the experimental average.

A flattening of the ion temperature profile is generally observed when reducing the temperature ratio boundary condition from  $T_i/T_e|_{\text{bc}} = 1.42$  to unity (see Fig. 10(c)). As the ion temperature gradient profiles corresponding to different values of  $T_i/T_e|_{\text{bc}}$  are usually quantitatively similar in the turbulence dominated region (cf. Fig. 11(c)), the reduction in on-axis ion temperature is partially attributed to a decrease of the boundary ion temperature. Still, in the region  $\rho_{\text{tor}} \in [0.35, 0.60]$ , where absolute gradients are steepest, a flattening of ion temperature gradients is observed for decreasing values of the temperature ratio boundary condition (cf. Fig. 11(c)). This effect is pronounced for temperature ratio boundary conditions close to unity, i.e.  $T_i/T_e|_{\text{bc}} \lesssim 1.1$ . Consequently, the decrease of on-axis ion temperature as  $T_i/T_e|_{\text{bc}}$  approaches unity is not solely due to a reduction in edge ion temperature. In the case of electron heat transport, electron temperature gradients are observed to behave similarly (see Fig. 11(b)), being roughly in agreement in the turbulent dominated region, yet exhibiting increased peaking with a reduction in the temperature ratio boundary condition, especially for  $T_i/T_e|_{\text{bc}} \lesssim 1.1$ .

In agreement with the observed density peaking as the temperature ratio boundary condition deviates significantly from unity, normalized density gradients are severely overestimated, exceeding experimental gradients by a factor of up to 4 (cf. Fig. 11(a)). Unlike normalized temperature gradients, normalized density gradients are highly sensitive to a reduction of the temperature ratio boundary condition, exhibiting noticeable flattening for each step in  $T_i/T_e|_{\text{bc}}$

---

<sup>3</sup>Note, that the plasma parameters illustrated in Fig. 10 do not represent the on-axis values of the respective profiles. Instead, the plasma response to a change in the  $T_i/T_e|_{\text{bc}}$  boundary condition is evaluated at  $\rho_{\text{tor}} = 0.41$ , corresponding to the innermost radial position where no additional transport is prescribed to mimic the effect of central MHD activity. As the respective transport coefficients are calculated to achieve central transport agreement for  $T_i/T_e|_{\text{bc}} = 1.10$ , predictive heat and particle transport simulations for deviating values of  $T_i/T_e|_{\text{bc}}$  do not necessarily yield central transport agreement. Thus in this analysis, plasma profiles inside  $\rho_{\text{tor}} \sim 0.4$  are subjected to both changing values of  $T_i/T_e|_{\text{bc}}$  and over-/underestimation of central MHD induced transport. Still, the plasma response observed at  $\rho_{\text{tor}} = 0.41$  is found qualitatively at all radial positions. Additionally, as the uncertainty of the regression results is increased on the magnetic axis (see Fig. 6), a comparison between the plasma response and the experimental average in terms of the respective standard deviation in the vicinity of the magnetic axis would demonstrate a higher degree of agreement than suggested by evaluation at mid-radius.

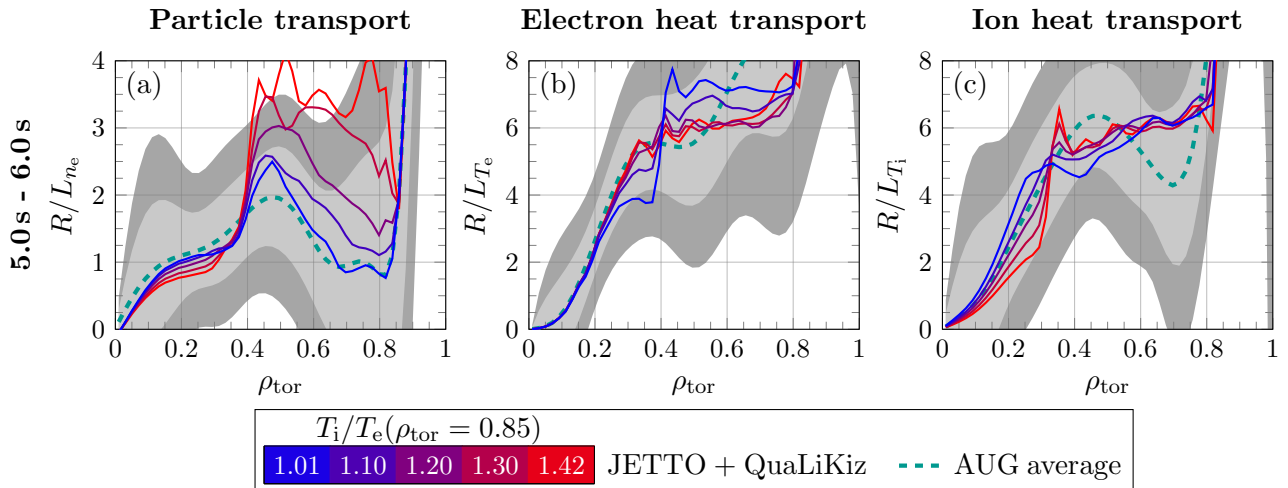


**Fig. 11:** Normalized plasma profile gradients for different values of the  $T_i/T_e|_{bc}$  boundary condition, gradually increasing from  $T_i/T_e|_{bc} = 1.01$  (blue) to 1.42 (red), for the time slice  $t_2 \in [5.0\text{ s}, 6.0\text{ s}]$ . From the temperature profiles obtained by Gaussian process regression ( $T_i/T_e|_{bc} = 1.42$ ), different ratios  $T_i/T_e|_{bc}$  are obtained by increasing  $T_e$  and reducing  $T_i$  by multiples of the respective standard deviations. Predicted normalized (a) electron density, (b) electron temperature and (c) ion temperature gradients compared to the experimental average (dashed green) with confidence intervals of  $1\sigma$  and  $2\sigma$  (grey).

performed. Furthermore, overestimation of density gradients is observed throughout the entire turbulence dominated region.

In the predictive heat and particle transport simulations carried out, plasma profiles are treated interpretively beyond  $\rho_{tor} = 0.85$ . As the plasma profiles evolved change gradually, the ion to electron temperature ratio is clamped in the vicinity of the simulation boundary, decreasing only slightly by typically  $\Delta T_i/T_e < 0.1$  down to the  $q = 1$  surface. The decrease of the temperature ratio across the turbulence dominated region is particularly low for values of the boundary condition noticeably exceeding unity. Under these conditions, a decrease of  $\Delta T_i/T_e < 0.05$  is observed as opposed to a decrease of  $\Delta T_i/T_e \sim 0.18$  in the case of equal edge temperatures. Consequently, the effect of an elevated temperature ratio boundary condition propagates inwards particularly well, thus reinforcing the decrease of particle transport in the turbulence dominated region.

As presented, increased density peaking is predicted by JETTO-QuaLiKiz for an ion to electron temperature ratio boundary condition significantly exceeding unity. A physical interpretation of this phenomenon is given in the next section.

### 5.1.2 Observations from gyrokinetic calculations

The impact of the ion to electron temperature boundary condition on both ion and electron scale turbulence present is analysed by stand-alone QuaLiKiz utilizing the converged plasma profiles calculated by JETTO-QuaLiKiz for different ratios  $T_i/T_e|_{bc}$ . Under these conditions, ion scale turbulence is stabilized qualitatively as the temperature ratio boundary condition is increased from unity up to the value  $T_i/T_e|_{bc} = 1.42$  obtained from Gaussian process regression (see Fig. 12(a)). In the latter case, the maximum instability growth rate is noticeably reduced. Additionally, turbulence is driven unstable over fewer wavenumbers. The opposite effect is observed for electron scale turbulence. As the temperature ratio boundary condition deviates progressively from unity, instability growth rates generally increase for all wavenumbers (see

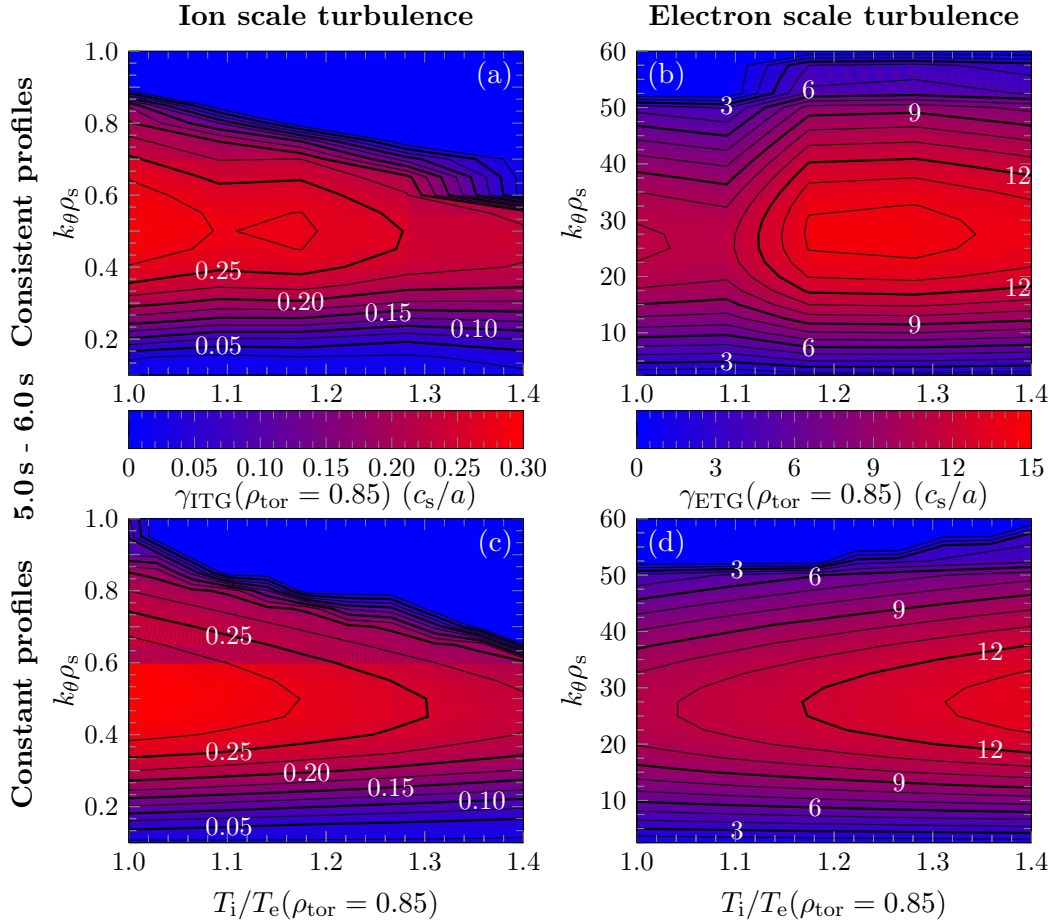


**Fig. 12:** Growth rates  $\gamma$  at the simulation boundary at  $\rho_{\text{tor}} = 0.85$  for (a,c) ion and (b,d) electron scale turbulence calculated by stand-alone QuaLiKiz for varying values of the  $T_i/T_e$  boundary condition using plasma parameters of the second time slice analysed. In (a,b), converged plasma profiles obtained with JETTO-QuaLiKiz for different values of  $T_i/T_e|_{\text{bc}}$  are used to calculate turbulence growth rates. In (c,d), plasma parameters from simulation results for  $T_i/T_e = 1.42$  are used for the same calculations with  $T_i/T_e$  set independently.

Fig. 12(b)), corresponding to an increase of electron scale turbulence.

Note, that converged self-consistent profiles of predictive heat and particle transport simulations are used as input for stand-alone QuaLiKiz. As a result, simulation parameters for different values of the temperature ratio boundary condition differ slightly in additional plasma parameters, most importantly in the normalized gradients prescribed. As the turbulence sensitivity analysis performed consequently does not solely depend on  $T_i/T_e|_{\text{bc}}$ , the growth rates calculated for both ion and electron scale turbulence do not change monotonously for all wavenumbers considered.

To emphasize the effect of a variation in the temperature ratio boundary condition, additional calculations are performed with QuaLiKiz, utilizing the converged profiles from predictive transport simulations for  $T_i/T_e|_{\text{bc}} = 1.42$  and manually adjusting boundary electron and ion temperature only. Consequently, all remaining plasma parameters are identically constant throughout this analysis, including the normalized gradients used. Following this approach, ion scale modes are found to be stabilized monotonously, electron scale modes destabilized monotonously as the temperature ratio increases (see Figs. 12(c,d)). Sensitivity of the growth rates on the ion to electron temperature ratio is expected as this dimensionless parameter is

introduced in the gyrokinetic dispersion relation solved by QuaLiKiz through summation of each particle species' Vlasov equation in the formulation of quasineutrality (cf. e.g. Eq. (4) in Ref. 20). A reduction of ITG modes with an increase in  $T_i/T_e$  is expected from analytical considerations, as the linear threshold for the emergence of these modes is shifted to larger values.<sup>45</sup> Similarly, the threshold of ETG modes is reduced under these conditions, resulting in a destabilization of electron scale modes as  $T_i/T_e$  is increased.<sup>46</sup>

Compared to the calculations performed using input parameters obtained from converged plasma profiles for all values of  $T_i/T_e|_{bc}$ , growth rates of both methods are in qualitative agreement. Consequently, the observed stabilization of ion scale modes and destabilization of electron scale modes when using plasma parameters from transport simulations can indeed be attributed to a change in  $T_i/T_e|_{bc}$  instead of an unfavourable change of the gradients prescribed.

Following the stabilization of ITG modes as the temperature ratio boundary deviates progressively from unity, a reduction in the particle diffusivity and the outward particle flux is observed for both cases, where either self-consistent or constant plasma profiles are used as input for stand-alone QuaLiKiz. Even though ETG modes are destabilized in the process, no increase in particle fluxes occurs as short wavelength turbulence does not drive particle transport. Consequently for temperature ratio boundary conditions significantly exceeding unity, turbulent particle transport is noticeably underestimated, resulting in the formation of peaked density profiles.

The electron temperature response to a variation of the temperature ratio boundary condition is determined by the collective effects of ITG stabilization and ETG destabilization. As the increase in electron heat transport driven by destabilized short wavelength turbulence outweighs the reduced drive due to ion scale turbulence stabilization significantly, electron heat transport is noticeably enhanced for values of  $T_i/T_e|_{bc}$  exceeding unity. Consequently, a reduction of the central electron temperature is observed.

In the case of ion heat transport, the stabilization of ITG modes with increasing temperature ratio boundary condition reduces turbulent contributions. As a result, ion temperature peaking is encountered. In contrast to the steady increase in core density as  $T_i/T_e|_{bc}$  progressively deviates from unity, the ion temperature response is stabilized at a constant level in predictive heat and particle transport simulations for  $T_i/T_e|_{bc} > 1.2$  due to heat exchange between ions and electrons. In the case of equal edge temperatures, net heat exchange is directed from the electron to the ion population. As the local ion temperature surpasses the local electron temperature as the temperature ratio boundary condition exceeds unity, the direction of net heat exchange reverses, transferring progressively more heat from ions to electrons. Consequently, further ion temperature peaking due to ITG stabilization and further electron temperature flattening due to ETG destabilization is countered by net ion to electron heat exchange. Therefore, heat transport predictions are less sensitive to temperature ratio boundary conditions noticeably exceeding unity. In the case of particle transport however, enhanced transport due to stabilization of ion scale turbulence is not compensated by another mechanism, resulting in the severe density peaking observed.

### 5.1.3 Significance of the boundary condition for predictive transport simulations

Applying the averaged profiles obtained by Gaussian process regression of raw experimental data to predictive heat and particle transport simulations, severe density peaking is observed as ITG turbulence is stabilized in the presence of an ion to electron temperature ratio at the

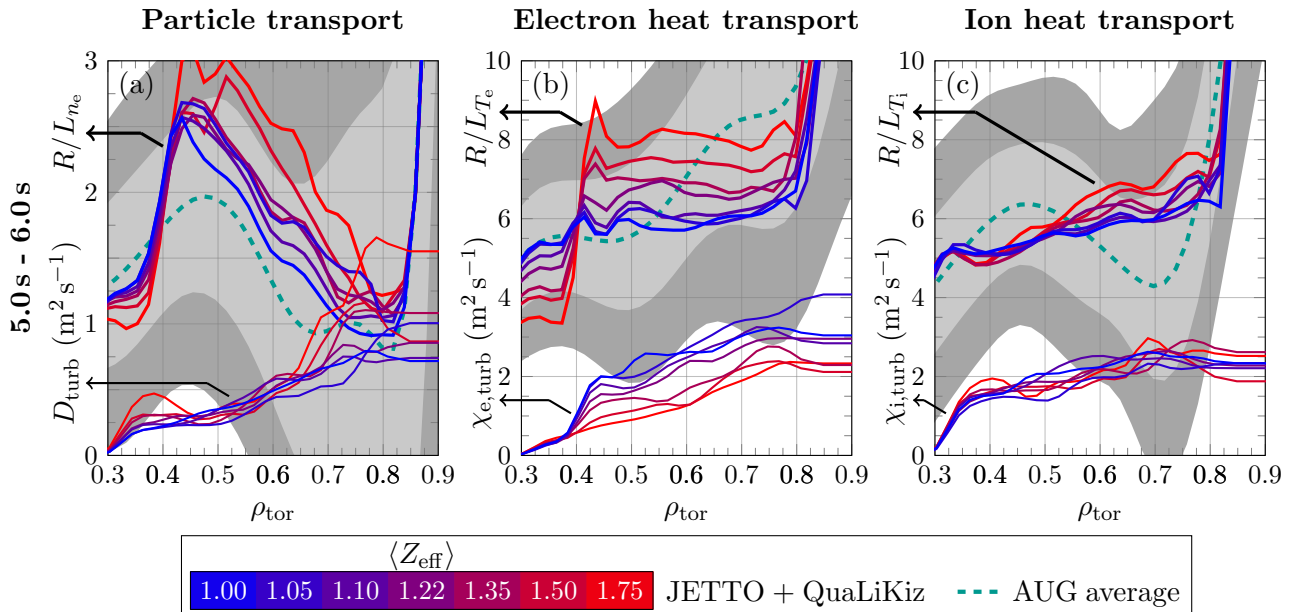


**Fig. 13:** Predictive particle and heat transport simulations for different values of the average effective charge  $\langle Z_{\text{eff}} \rangle$ , gradually increasing from  $\langle Z_{\text{eff}} \rangle = 1.00$  (blue) to 1.75 (red). Normalized gradients (solid, thick) of the (a) electron density, (b) electron temperature and (c) ion temperature are compared to the experimental average (dashed green) with confidence intervals of  $1\sigma$  and  $2\sigma$  (grey). Corresponding transport coefficients (solid, thin) in (a-c) are averaged over the last 0.25 s of steady-state plasma evolution to account for fluctuations in these parameters.

simulation boundary of  $T_i/T_e|_{\text{bc}} = 1.42$ . However, as regression results are subjected to uncertainties just as the raw data they are based upon, reasonable adjustments of the temperature profiles at the simulation boundary are carried out under consideration of the uncertainties mentioned. Simulations using the improved boundary conditions are found to agree significantly better with experimental profiles without resorting to unjustifiable modifications to the transport calculations. Hence, the choice of the boundary conditions used is crucial for the success of transport simulations.

The analysis of raw experimental data from multiple diagnostics is not only important to constrain the boundary conditions within reasonable bounds, but also to allow for a reliable comparison of simulation results and is thus encouraged as good practice. Furthermore, as different regression techniques apply different weights to the raw data, emphasize different regions of the plasma, assume different underlying functions or operate intentionally with a different degree of accuracy, the preparation of averaged plasma profiles specifically for the simulation to be carried out is highly recommended. The use of a probabilistic approach is suggested to avoid applying (unconscious) bias to major aspects of data regression.

## 5.2 ETG stabilization by impurities

Simulation results are found moderately sensitive to the average effective charge prescribed for this discharge<sup>4</sup>. With an increase in impurity content, peaking of all main plasma profiles is observed, as illustrated by the corresponding normalized gradients in Fig. 13. A noticeable reduction in electron heat transport is achieved with the introduction of additional C-impurities,

<sup>4</sup>Note, that the density profile of C-impurities present is evolved by SANCO throughout the entire plasma from a radially constant profile, reaching steady state within 0.2 s of plasma evolution.

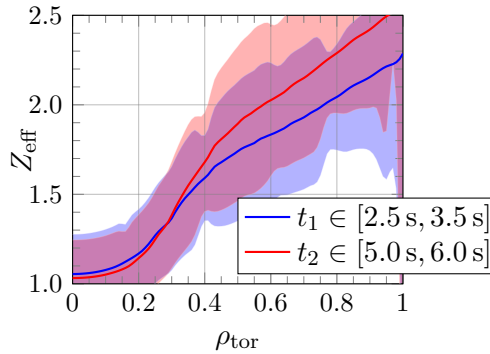


**Fig. 14:** The effective charge  $Z_{\text{eff}}$  derived from Bremsstrahlung measurements in both time slices  $t_1 \in [2.5 \text{ s}, 3.5 \text{ s}]$  (blue) and  $t_2 \in [5.0 \text{ s}, 6.0 \text{ s}]$  (red) is incompatible with estimates of  $\langle Z_{\text{eff}} \rangle = 1.22$  from impurity density analysis by CXRS.

resulting in monotonously increasing gradients in the turbulence dominated region for all values of  $\langle Z_{\text{eff}} \rangle$  considered (see Fig. 13(b)). With respect to the simulations performed for a pure deuterium plasma, on-axis electron temperature is increased by 0.7 keV (+20%) when applying an effective charge of 1.75. Both particle and ion heat transport are less affected, as respective profiles are found increased by around 10% ( $+0.7 \times 10^{19} \text{ m}^{-3}$ ,  $+0.4 \text{ keV}$ ) under these conditions. Correspondingly, variations in normalized gradients predicted are less distinct, yet clearly present (see Figs. 13(a,c)).

Analysing the influence of microturbulence on the profile peaking observed, turbulent electron heat transport is significantly reduced when the impurity content increases progressively, as demonstrated by the change in turbulent heat diffusivity (see Fig. 13(b)). In the case of the highest average effective charge of  $\langle Z_{\text{eff}} \rangle = 1.75$  considered, heat diffusivity is reduced by around  $1.0 \text{ m}^2 \text{ s}^{-1}$  throughout the turbulence dominated region as compared to the situation of a pure deuterium plasma. Simultaneously, no clear change in neither particle nor ion heat turbulent transport coefficients is generally observed for an increase in the average effective charge applied (see Fig. 13(a,c)). Turbulent transport coefficients corresponding to either end of the scan in  $\langle Z_{\text{eff}} \rangle$  are found approximately in agreement. If anything, an increase in turbulent particle and ion heat diffusivities is predicted in the vicinity of the  $q = 1$  surface and close to the pedestal shoulder.

As only turbulent electron heat transport is noticeably affected by an increase in impurity content, ETG modes are found stabilized under these conditions. Consequently, steep electron temperature gradients are required to reach the instability threshold in agreement with expectations,<sup>46</sup> resulting in a peaked electron temperature profile. In this process, the significant net heat exchange from ions to electrons in the case of a pure deuterium plasma is steadily reduced, reversing direction to net ion heating for  $\langle Z_{\text{eff}} \rangle \geq 1.35$ . The resulting peaking in ion temperature is sufficient to drive ITG modes further unstable, countering the ITG stabilization by an increase in  $\langle Z_{\text{eff}} \rangle$ , thus leaving these modes roughly unaffected. These observations are confirmed by stand-alone QuaLiKiz using the converged profiles of predictive simulations with JETTO-QuaLiKiz. The density peaking observed is driven by a significant increase in the inward neoclassical pinch, ranging from around  $2 \text{ cm s}^{-1}$  for a pure deuterium plasma to just  $10 \text{ cm s}^{-1}$  when applying  $\langle Z_{\text{eff}} \rangle = 1.75$ .

Applying an average effective charge around 1.2 to the simulations as suggested by the preceding discharges #31113 and #31114, excellent agreement between predictive heat and particle

transport simulations and the experimental average described in Sec. 4.1 is achieved. Data from Bremsstrahlung measurements available for this discharge imply a significantly elevated average effective charge in the order of  $\langle Z_{\text{eff}} \rangle \gtrsim 1.8$  for both phases of the discharge (see Fig. 14). Deviations from the value suggested by impurity density analysis from CXRS are even more pronounced in the second time slice analysed. Under these conditions on-axis electron density and temperature peaking above experimental levels is observed, thus strongly suggesting the use of the average effective charge of preceding discharges instead of values obtained through Bremsstrahlung measurements. Even though other parameters of the simulations presented are similarly subject to increased uncertainty, such as the ion to electron temperature ratio at the simulation boundary, the choice of  $\langle Z_{\text{eff}} \rangle = 1.22$  throughout this study cannot be attributed to favourable conditions used for  $T_i/T_e|_{\text{bc}}$ . Applying the original value of  $T_i/T_e|_{\text{bc}} = 1.42$ , severe density peaking is obtained for any choice of the average effective charge. Using equal edge temperatures however, the on-axis electron temperature is highly elevated for any choice of  $\langle Z_{\text{eff}} \rangle$  approaching the value suggested by Bremsstrahlung measurements. Consequently, the average effective charge used throughout this study can be considered accurate within reason.

### 5.3 Core density dependence on NBI fuelling

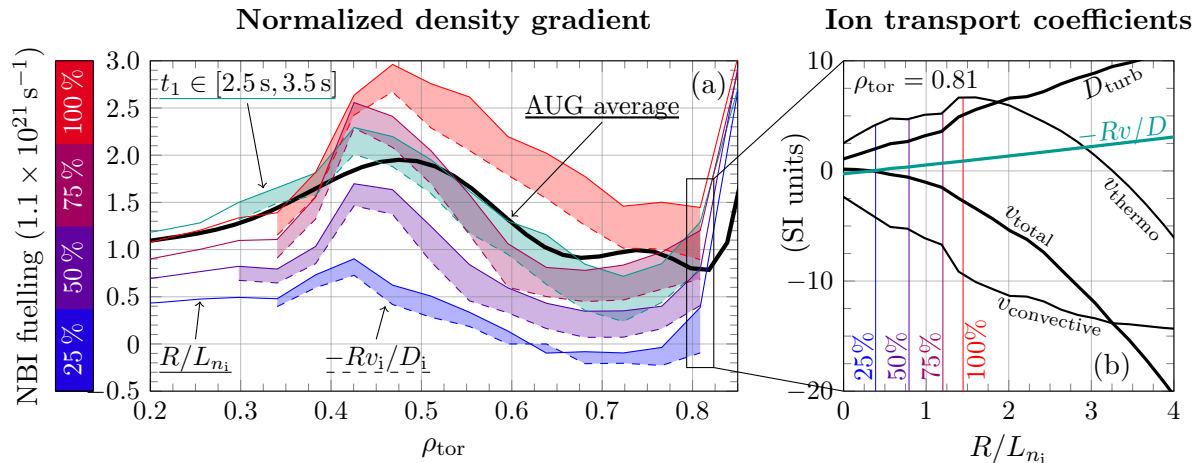
At  $t = 3.5$  s of the discharge, an additional 60 kV NBI injector is coupled to the plasma, supplementing the three sources already employed. In the process, plasma fuelling and heating are increased by  $3.1 \times 10^{20} \text{ s}^{-1}$  and 2.4 MW, respectively. Simultaneously, a transition in central MHD activity from sawteeth to a continuous (1, 1) mode is observed. Under these conditions, the electron density is slightly decreased by  $(0.25 \pm 0.03) \times 10^{19} \text{ m}^{-3}$  at all radial positions of the core plasma ( $-3.3\%$  on-axis), as captured by measurements from TS and LIB (see Fig. 6(a,i)). Correspondingly, gradients change only to a minor extent between both phases of the discharge, being virtually unaltered in the turbulence dominated region. A slight decrease in core electron density is regularly observed in AUG H-mode discharges when auxiliary heating is provided to a larger fraction by NBI as compared to the contributions of ECRH to total heating.<sup>47,48</sup>

The minor reduction in plasma density observed experimentally is not described by the predictive heat and particle transport simulations performed. Instead, an increase in density peaking is predicted in the second time slice (see Fig. 15(a)). Analysing the relevant contributions of the steady state particle balance

$$R/L_n = \frac{R S_n}{nD} - \frac{Rv}{D} \quad (5)$$

in the presence of a source  $S_n$ , the ratio of convective to diffusive main ion transport in the turbulence dominated region increases in the second phase of the discharge (see Fig. 15(a)) since the increase in the inward pinch outweighs the general increase of the diffusivity. Simultaneously, the stronger source  $S_n$  is countered by the increased diffusivity and density. This suggests that the increase in  $R/L_n$  in the second phase of the discharge is primarily driven by an over proportional increase of the turbulent inward pinch. Note that only turbulent contributions to the total inward pinch and diffusivity are considered as neoclassical contributions are negligible ( $v_{\text{nc}} \sim -0.05 \text{ m s}^{-1}$ ,  $D_{\text{nc}} \sim 0.02 \text{ m}^2 \text{ s}^{-1}$ ).

Performing simulations of the second phase of the discharge with a particle source artificially reduced to 75%, mimicking the source of time slice  $t_1$ , good agreement in particle transport is achieved in the turbulence dominated region as compared to the experimental average (see



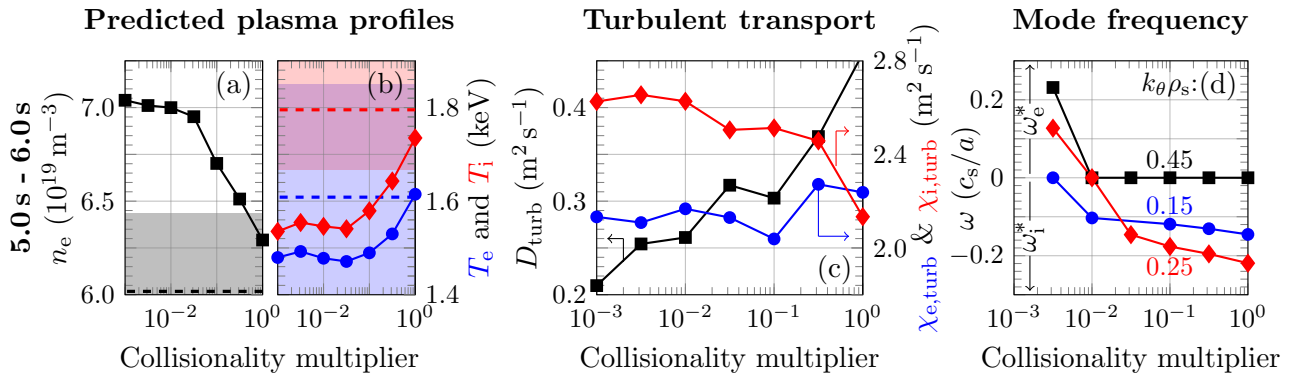
**Fig. 15:** Predictions by JETTO-QuaLiKiz in the time slice  $t_2 \in [5.0 \text{ s}, 6.0 \text{ s}]$  for varying amounts of NBI fuelling (between one and four averaged NBI injectors; coloured blue to red) of (a) the core main ion density gradient  $R/L_{n_i}$  (solid) compared to the experimental average (thick black) and to the ratio of turbulent convective to turbulent diffusive main ion transport  $-Rv_i/D_i$  (dashed) in each case. The difference (shaded) between predicted  $R/L_{n_i}$  and  $-Rv_i/D_i$  denotes the source term (cf. Eq. (5)). The same is additionally shown for time slice  $t_1 \in [2.5 \text{ s}, 3.5 \text{ s}]$  utilizing three NBI injectors. (b) Main ion transport coefficients calculated by stand-alone QuaLiKiz at  $\rho_{\text{tor}} = 0.81$  for varying  $R/L_{n_i}$ : turbulent diffusivity  $D_{\text{turb}}$ , thermodiffusive pinch  $v_{\text{thermo}}$ , pure convective term  $v_{\text{convective}}$ , total pinch  $v_{\text{total}}$ , as well as the ratio of turbulent convective to turbulent diffusive transport  $-Rv_i/D_i$  (green). The values of  $R/L_{n_i}$  ( $\rho_{\text{tor}} = 0.81$ ) of the JETTO-QuaLiKiz simulations in Fig. 15(a) are highlighted (vertical, coloured).

Fig. 15(a)). Note that transport agreement inside the  $q = 1$  surface is not obtained, since additional transport coefficients prescribed are tailored for simulations incorporating the full particle source. Utilizing only one or two average NBI injectors in the presence of the full 10 MW of NBI heating, a further flattening of the electron density profile is predicted, highlighting the sensitivity of the simulations on the particle source employed. With a progressive reduction of the the particle source throughout this analysis, a minor increase in both electron and ion temperature occurs, accompanied by a subtle reduction in turbulent heat diffusivity.

Reducing only the particle source in the second phase of the discharge, the ratio of turbulent convective to turbulent diffusive main ion transport decreases significantly, yet still constitutes the dominant contribution to the predicted normalized density gradient (see Fig. 15(a)). Simulations by stand-alone QuaLiKiz of the steady-state solution obtained with JETTO-QuaLiKiz identify a strong sensitivity of both the thermodiffusive pinch and the pure convective term on the particle source  $S_n$  employed, or rather on the normalized density gradient  $R/L_n$  as observed in additional simulations with stand-alone QuaLiKiz where only  $R/L_n$  was modified (see Fig. 15(b)). The latter simulations suggest an increased sensitivity of the density predictions on the source term through modification of the initial  $R/L_n$  and thus of the aforementioned pinches. This sensitivity will be investigated in the future in more detailed comparison with gyrokinetic modelling.

#### 5.4 Particle transport reduction with reduced collisionality

In this study, the effect of a reduction in the collisionality utilized in QuaLiKiz on core profile agreement was additionally analysed to assess the possibility of particle transport enhancement in the presence of an elevated ion to electron temperature ratio  $T_i/T_e|_{\text{bc}}$  at the boundary



**Fig. 16:** Predictive heat and particle transport simulations performed by JETTO-QuaLiKiz by progressively reducing a multiplier in the calculation of the collisionality used in QuaLiKiz at  $\rho_{\text{tor}} = 0.58$  in the second time slice  $t_2 \in [2.5, 3.5]$  s. Calculated (a) electron density (black squares), (b) electron temperature (blue circles), and ion temperature (red diamonds) compared to the respective experimental averages (dashed, same colour) and associated uncertainties of  $1\sigma$ . Turbulent (c) particle transport (squares, left ordinate), electron heat (circles) and ion heat (diamonds) transport coefficients of the profiles shown in (a, b). (d) Frequency of three different long wavelength modes. Note, that the ion diamagnetic drift frequency  $\omega_i^*$  is defined negative, whereas the electron diamagnetic drift frequency  $\omega_e^*$  is defined positive in QuaLiKiz.

condition. Although the significant deviation from a temperature ratio boundary condition of unity was identified as the reason for core particle transport underprediction, the influence of a change in collisionality on transport predictions is repeated for the set of parameters used throughout this study. For this purpose, an additional free parameter is introduced in the calculation of the collisionality. Consequently, consistent evaluation of the collisionality in accordance with plasma parameters is ensured, yet allowing for an arbitrary modification of collisionality.

Reducing the multiplier from unity down to  $10^{-3}$ , an increase in electron density well above experimental levels is observed in the turbulence dominated region (see Fig. 16(a)), corresponding to an overprediction of around  $2\sigma$  of the regression uncertainties for the lowest values of the multiplier applied. Simultaneously, a decrease in both electron and ion temperature below the experimental average occurs in the same region (see Fig. 16(b)). In the case of ion heat transport, temperatures are underestimated by just below  $2\sigma$  using multipliers in the order of  $10^{-3} - 10^{-2}$ . Noticeably, plasma profiles are most sensitive to a change in the collisionality multiplier for values above  $10^{-2}$ . Considering the turbulent contributions to transport (see Fig. 16(c)), particle diffusivity is strongly reduced in the range of multipliers covered, explaining the increase in electron density predicted. Similarly, the decrease in ion temperature is due to an increase in ion heat transport. Turbulent electron heat transport however is virtually unaffected by a reduction of the collisionality multiplier. Instead, ion to electron heat exchange becomes less important as the ion temperature decreases, resulting in a reduction of electron temperature.

Under conditions of strongly reduced collisionality, ion scale modes are found more unstable as in the default case. Consequently, ion heat transport is increased. With a reduction in collisionality, de-trapping of electrons in banana orbits is less efficient, resulting in an overall decrease of particle transport. Simultaneously, the emergence of TEM modes is predicted by QuaLiKiz whereas ITG modes are found stable (see Fig. 16(d)) in the presence of a larger pop-

ulation of trapped electrons. Increasing the collisionality multiplier, the system moves deeper into the ITG regime, as indicated by the increase in mode frequency in the ion diamagnetic drift direction. Reproduction of increased density peaking with reduced collisionality as the mode frequency becomes closest to zero in absolute terms is in agreement with other works,<sup>49</sup> thus increasing the confidence in the applicability of the reduced gyrokinetic code QuaLiKiz.

Even though the heat and particle transport predictions performed are found sensitive to the value of the collisionality multiplier used, the good agreement between simulations and experiment discussed in Sec. 4.1 is obtained only when imposing a collisionality multiplier close to its default value of unity. Since the quasilinear fluxes calculated by QuaLiKiz were validated using JET parameters, applicability of the Krook collision operator used in QuaLiKiz<sup>50</sup> to conditions of AUG discharges is an additional success for the reduced code QuaLiKiz.

## 6 Predictive trace W impurity transport simulations

Transport of trace amounts of W impurities in typical AUG or JET discharges is determined by both neoclassical and turbulent effects. Since W transport is thus influenced by the main ion density and temperature profiles, successful modelling of the corresponding transport channels is a vital prerequisite for accurate trace W transport simulations. As demonstrated in the first part of this study (see Sec. 4.1), JETTO-QuaLiKiz are found to be capable of correctly predicting main plasma profiles of AUG discharge #31115, thus paving the way for transport simulations of trace amounts of W impurities.

Predictive trace W transport simulations are performed with the impurity transport code SANCO within JETTO. In the trace limit, W impurities are assumed not to influence the evolution of main ion profiles. Hence, the impurity radiation calculated by SANCO is not used to solve the energy balance equations. Instead, converged plasma profiles obtained through predictive modelling with JETTO-QuaLiKiz under consideration of experimental measurements of impurity radiation are used interpretively. The temporal evolution of the W density is simulated over 1 s to ensure reaching steady-state conditions. Turbulent contributions to W transport are calculated by QuaLiKiz, taking poloidal asymmetries of trace impurities into account. To account for neoclassical transport in the presence of rotation induced poloidal asymmetries of the W density distribution, the code NEO<sup>51,52</sup> is used. To assess the significance of neoclassical, turbulent and MHD driven transport for the avoidance of central W accumulation, three cases are modelled. In each simulation, the impact of MHD activity on an increasing number of transport channels is considered:

- 1) no transport channels affected
- 2) main ion heat and particle transport affected
- 3) W impurity, main ion heat and main ion particle transport affected

Remaining simulation parameters are kept identical throughout this analysis. The influence of central MHD activity on W impurity transport is expressed as a pinch velocity through  $v_{\text{MHD}} = -D_{\text{MHD}} \nabla_{\rho} n_e / n_e$ . The diffusivity  $D_{\text{MHD}}$  attributed to MHD activity was prescribed in predictive main ion heat and particle transport simulations inside  $\rho_{\text{tor}} = 0.4$  to force agreement between simulated and effective main ion particle transport. For the calculation of the MHD driven outward pinch velocity, the steady-state density profiles predicted by JETTO-QuaLiKiz are used. The impact of MHD activity on different transport channels is taken as either convective (W impurities) or diffusive (main ion heat and particles) based on technical reasons only. Expressing the effect of central MHD activity in terms of a pinch velocity  $v_{\text{MHD}}$  instead of

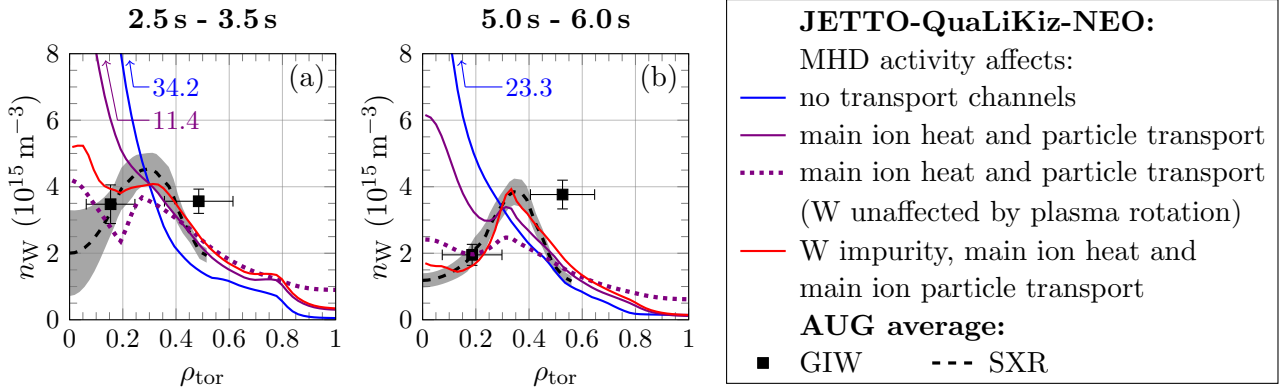


**Fig. 17:** W density profiles predicted by JETTO-QuaLiKiz-NEO (coloured) in both time slices (a)  $t_1 \in [2.5\text{ s}, 3.5\text{ s}]$  and (b)  $t_2 \in [5.0\text{ s}, 6.0\text{ s}]$  compared to the experimental average derived from grazing incidence spectrometry (GIW, squares) and soft X-ray spectroscopy (SXR, dashed) measurements and the corresponding uncertainties of  $1\sigma$ . Simulations are carried out neglecting the effect of MHD activity on both main ion and W transport (blue), considering only the influence on main ion heat and particle transport (purple) or considering the effect of MHD activity on W impurity, main ion heat and main ion particle transport (red). In additional simulations, plasma rotation is omitted (dotted) to illustrate the influence of poloidal asymmetries on the W density response.

a diffusivity  $D_{\text{MHD}}$ , consistent results for the main ion heat and particle transport simulations are obtained. Following this approach, the effect of central MHD activity is assumed to be identical for deuterium and W ions.

Neglecting the influence of MHD driven transport on both W impurity transport and main ion transport, significant central W accumulation inside  $\rho_{\text{tor}} = 0.3$  is predicted in qualitative disagreement with experimental measurements for both time slices analysed (see Fig. 17). As the central hollow W density profile captured by SXR is not reproduced by NEO under these conditions, on-axis W density is overpredicted by an order of magnitude. In both cases, strong inward neoclassical pinches are predicted inside the  $q = 1$  surface, leading to severe central W accumulation. Since measurements by SXR suggest a reduction of the total W content in the plasma by around 30% with the onset of the continuous (1, 1) MHD mode in the second phase of the discharge, the on-axis W density predicted in the second time slice is reduced with respect to the value calculated for the first phase, despite the presence of a stronger net inward neoclassical pinch. It should be noted, that even after 1 s of W density evolution under these conditions, a steady-state solution is not obtained. Instead, central W impurity content is predicted to increase further above the levels shown in Fig. 17.

Considering the indirect effect of MHD activity inside the  $q = 1$  surface at  $\rho_{\text{tor}} \sim 0.4$  on central W accumulation through modification of main ion temperature and density profiles, neoclassical W impurity transport is insufficient to establish a hollow W profile in either of the time slices analysed. Instead, a peaked W density profile is predicted in both cases, noticeably exceeding experimental measurements (see Fig. 17).

To assess the relevance of poloidal asymmetries on neoclassical W transport in the case of MHD enhanced main ion heat and particle transport, simulations are repeated neglecting the influence of rotation under otherwise identical conditions. In both time slices analysed, a comparatively flat central W density is predicted (see Fig. 17), due to a transition from negative to positive W density gradients at  $\rho_{\text{tor}} \sim 0.2$ . Inside this location, inward neoclassical convection dominates neoclassical W transport due to the low amplitude of the ion temperature

gradient. For larger radial positions, the effect of temperature screening dominates over the inward pinch, resulting in the generation of positive  $W$  density gradients. Noticeably, inside  $\rho_{\text{tor}} \sim 0.3$ , simulations by NEO in the absence of poloidal asymmetries are in qualitative agreement with analytical considerations of neoclassical  $W$  transport (see Fig. 4(a)). At radial positions exceeding  $\rho_{\text{tor}} \sim 0.3$  turbulent transport sets in, re-establishing negative  $W$  density gradients. The shape of the resulting density profile is thus in close agreement with experimental observations for  $\rho_{\text{tor}} \gtrsim 0.2$  (where available). Importantly, on-axis  $W$  behaviour is predicted qualitatively incorrect with respect to experimental observations.

The central  $W$  behaviour calculated by NEO in the absence of poloidal asymmetries is in qualitative disagreement with predictions taking centrifugal effects into account (see Fig. 17). In the presence of plasma rotation, the impact of temperature screening is significantly reduced, as indicated by the absence of positive  $W$  density gradients, thus highlighting the relevance of rotational effects. Consequently, the  $W$  density distribution is strongly asymmetric in the poloidal plane in both phases of the discharge. Consideration of centrifugal effects on heavy impurity transport is therefore mandatory.

Qualitative agreement between experiment and predictive  $W$  impurity transport simulations with NEO is achieved only when considering the direct impact of central MHD activity on both  $W$  and main ion transport (see Fig. 17). In the presence of the continuous  $(1, 1)$  mode, a deeply hollow  $W$  profile is predicted, capturing excellently the behaviour measured by SXR. However, the experimental conditions in the presence of sawteeth are only reproduced for  $\rho_{\text{tor}} \gtrsim 0.2$ . Inside, slight on-axis  $W$  peaking is predicted, whereas a hollow  $W$  density profiles is measured on average in this phase of the discharge. Yet, compared to simulations considering only the influence of MHD activity on main ion transport, central  $W$  content is significantly reduced. As simulations by NEO are thus much closer to experimental conditions in the presence of MHD driven  $W$  impurity transport, the direct influence of central MHD activity on  $W$  transport is crucial to reduce or even avoid central  $W$  accumulation.

The disagreement of central  $W$  behaviour between predictions by NEO and measurements by SXR in the first time slice may be related to inaccuracies in describing the effect of a sawtooth cycle by a constant, averaged transport coefficient. Experimentally, flattening of both peaked main ion and hollow  $W$  density profiles is observed during a sawtooth crash, pointing to a strong diffusive rather than a convective effect of sawteeth. Given the rapid redistribution of heat and particles, neoclassical  $W$  impurity transport is expected to change drastically throughout a sawtooth cycle. Hence, simulations of plasma conditions averaged over several sawtooth cycles may not capture the averaged effect of sawteeth accurately. The  $W$  density response throughout a sawtooth cycle will be examined in future work.

The assumption of deuterium and  $W$  ions being equally affected by the convective effect of the continuous  $(1, 1)$  MHD activity led to excellent agreement between central  $W$  density predictions and experiment. Introducing a dependence on solely the ion mass or charge would significantly modify  $W$  pinch velocities, resulting in either the irrelevance or complete dominance of MHD driven outward  $W$  impurity transport. Considering the uncertainties of the simulation results, a dependence on the charge to mass ratio cannot be discarded due to a differences of only a factor 2 comparing both ion species under the present conditions. However, the tools used in this study are not suitable to accurately determine the effect of MHD activity on  $W$  impurities. Further investigation of directly driven MHD  $W$  impurity transport in an integrated framework is thus necessary (for work on non-integrated modelling see e.g. Refs. 53–56). Following the

promising predictions of central W behaviour by NEO, the pinch velocities prescribed are likely in the correct order of magnitude.

## 7 Summary and outlook

In this study, integrated modelling of main ion heat and particle transport in AUG discharge #31115 was carried out by JETTO-QuaLiKiz for the first time. Excellent agreement between simulations and experiment is found for all transport channels, with average deviations of plasma profiles and associated gradients being in the order of 1 – 6% and 10 – 30% respectively. While the quasilinear turbulent fluxes calculated by QuaLiKiz have been validated against JET discharges,<sup>20</sup> correct reproduction of experimental conditions in the mid-sized tokamak ASDEX Upgrade demonstrates the capabilities of the reduced model QuaLiKiz. The temperature and density profiles calculated by JETTO-QuaLiKiz are also obtained utilizing ASTRA+QuaLiKiz. For practical purposes, this benchmark between both implementations of QuaLiKiz is excellent. Consequently, the very fast quasilinear gyrokinetic code QuaLiKiz can be utilized for the calculation of turbulent fluxes in integrated transport simulations with even more increased confidence.

Thorough analysis and careful interpretation of experimental measurements proved crucial for successful prediction of transport in the turbulence dominated region between the  $q = 1$  surface at  $\rho_{\text{tor}} \approx 0.4$  and the fixed boundary condition at  $\rho_{\text{tor}} = 0.85$ . Utilizing raw ion and electron temperature measurements without further analysis, an averaged ion to electron temperature ratio significantly exceeding unity is prescribed at the boundary condition. Under these conditions, ITG modes are stabilized and particle transport severely underpredicted as a result. A comparable underprediction of ion heat transport is not observed due to increased net ion to electron heat transfer, as ETG modes are additionally destabilized. Through application of Gaussian process regression techniques, reliable estimates of plasma profiles and corresponding uncertainties are obtained from experimental data, allowing prescription of more reasonable boundary conditions, thus yielding the good agreement between simulations and experiment described. As the validation and interpretation of experimental measurements is vital for simulation success, following this approach is strongly encouraged as good practice.

Central transport inside the  $q = 1$  surface is dominated by MHD activity, being sawteeth and a continuous  $(m, n) = (1, 1)$  mode in different phases of the discharge. To achieve central transport agreement, additional transport coefficients derived from balance equations are prescribed to the simulations performed. Noticeably, the impact of the  $(1, 1)$  MHD mode on transport is stronger, exhibiting increased flattening of central temperature profiles.

Simulations of trace W impurity transport based on the successful modelling of main ion heat and particle transport are capable of qualitatively reproducing central hollow W density profiles measured in the presence of the continuous  $(1, 1)$  MHD mode. Neglecting the impact of MHD activity on both main ion and heavy impurity transport, strongly peaked central W density profiles are predicted by neoclassical heavy impurity transport under consideration of poloidal asymmetries. The impact of MHD on only the main ion profiles is insufficient to create conditions of reversed net neoclassical heavy impurity transport in AUG discharge #31115. Instead, qualitative agreement with experimental measurements is obtained only when subjecting trace W impurities to the impact of the continuous  $(1, 1)$  MHD mode directly.

The impact of MHD activity on central transport is derived from balance equations only in this study. However, to advance predictive integrated modelling of discharges such as AUG

#31115, an accurate first-principles based reduced model of MHD driven transport is necessary for all transport channels. Regarding the influence of the (1, 1) MHD mode on heavy impurity transport, several questions need further attention:

- Is the outward trace W impurity transport due to the direct effect of the saturated (1, 1) MHD mode or due to the direct effect of ECRH?
- Is the outward pinch assumed for the MHD transport identical for both W trace impurities and main ions (as assumed for consistency in this study)?
- Are further contributions to central W trace impurity transport necessary to match experimental measurements?

### Acknowledgements

This work has been carried out within the framework of the EUROfusion Consortium and has received funding from the Euratom research and training programme 2014-2018 under grant agreement No 633053. The views and opinions expressed herein do not necessarily reflect those of the European Commission. DIFFER is a partner in the Trilateral Euregio Cluster TEC.

### A Overview of JETTO-QuaLiKiz simulations and versions used

The simulations presented throughout this work were carried out on the Freia cluster of the UK Atomic Energy Authority (UKAEA) and are accessible through the local catalogue manager and the Processed Pulse File (PPF) system. Catalogue entries and PPF sequence numbers are provided in Table 2 for each simulation discussed.

Throughout the course of this work, new versions of JETTO-QuaLiKiz have been introduced. The overview of simulations performed is given separated by version and in order of release. Note, that the simulations presented in Sec. 4.1, performed with version 83e0078788, were repeated with each major release (8c0622caed, edb9ddab05) to ensure validity of the results. The aforementioned JETTO versions used are defined by the first 10 digits of the corresponding git SHA1-key.

During finalization of this study, the interface between QuaLiKiz and JETTO was updated to version 7b7f3ea091 to calculate the  $E \times B$  shearing rate directly from

$$\gamma_{E \times B} = -\frac{r}{q} \frac{d}{dr} \left( \frac{q}{Br} \underbrace{\left[ v_\varphi B_\theta + \frac{d}{dr} p_i - v_\theta B_\varphi \right]}_{E_r} \right), \quad (6)$$

where the quantity  $r$  denotes the midplane average radial coordinate, instead of utilizing internal JETTO estimations of  $\gamma_{E \times B}$ . Following this update, stabilization of ion scale turbulence in the vicinity of the pedestal region and consequently a noticeable overprediction of density profiles throughout the entire radius was initially observed in the AUG discharge analysed when applying identical settings as in the heat and particle transport simulations discussed in Sec. 4.1.

Good agreement between simulations and experiment is recovered by minor modifications to the ion pressure profile well within experimental uncertainties in the vicinity of the simulation boundary. By ensuring a constant ion pressure gradient in the initial step of the simulation, a negative feedback loop of increasing  $E \times B$  shear due to profile changes over short spatial scales is avoided. In the case of the second time slice analysed, a reduction of the toroidal velocity gradient within experimental uncertainties was additionally performed in the vicinity

**Table 2:** The simulations presented throughout this work are accessible through the local catalogue manager or the PPF system on the Freia cluster of the UKAEA. Throughout the course of this work, new versions of JETTO-QuaLiKiz have been introduced, defined below by the first 10 digits of the corresponding git SHA1-key. Validity of previous results was confirmed by re-running the default simulations with each new version released.

Section	Catalogue entry	PPF seq num	Time	Description
	<i>olinder/jetto/aug/31115/</i>	<i>shot = 31115</i>	<i>slice</i>	
		<i>userid = olinder</i>		
<b>Simulations with 83e0076788</b>				
4.1	jul1017/seq#1	#91	$t_1$	default simulation
	jul1217/seq#1	#92	$t_2$	default simulation
	jul2017/seq#1	#93	$t_1$	w/o MHD transport
	jul2017/seq#2	#94	$t_2$	w/o MHD transport
5.1	jul1317/seq#1	#95	$t_2$	$T_i/T_e _{bc} = 1.42$
	jul1317/seq#2	#96	$t_2$	$T_i/T_e _{bc} = 1.30$
	jul1317/seq#3	#97	$t_2$	$T_i/T_e _{bc} = 1.10$
	jul1317/seq#4	#98	$t_2$	$T_i/T_e _{bc} = 1.01$
5.2	jul1717/seq#1	#99	$t_2$	$Z_{\text{eff}} = 1.001$
	jul1717/seq#2	#100	$t_2$	$Z_{\text{eff}} = 1.05$
	jul1717/seq#3	#101	$t_2$	$Z_{\text{eff}} = 1.10$
	jul1717/seq#4	#102	$t_2$	$Z_{\text{eff}} = 1.35$
	jul1717/seq#5	#103	$t_2$	$Z_{\text{eff}} = 1.50$
	jul1717/seq#6	#104	$t_2$	$Z_{\text{eff}} = 1.75$
5.3	jul2517/seq#1	#105	$t_2$	NBI fuelling: 75%
	jul2517/seq#2	#106	$t_2$	NBI fuelling: 50%
	jul2517/seq#3	#107	$t_2$	NBI fuelling: 25%
5.4	jul2517/seq#4	#108	$t_2$	collisionality: $3.16 \times 10^{-1}$
	jul2517/seq#5	#109	$t_2$	collisionality: $1.00 \times 10^{-1}$
	jul2517/seq#6	#110	$t_2$	collisionality: $3.16 \times 10^{-2}$
	jul2517/seq#7	#111	$t_2$	collisionality: $1.00 \times 10^{-2}$
	jul2517/seq#8	#112	$t_2$	collisionality: $3.16 \times 10^{-3}$
	jul2517/seq#9	#113	$t_2$	collisionality: $1.00 \times 10^{-3}$
<b>Simulations with 8c0622caed</b>				
6	aug2917/seq#1	#114	$t_1$	W transp. w/o any MHD
	sep0117/seq#1	#115	$t_2$	W transp. w/o any MHD
	aug2717/seq#1	#116	$t_1$	W transp. w/o MHD, rotation
	aug2417/seq#1	#117	$t_2$	W transp. w/o MHD, rotation
	aug2417/seq#2	#118	$t_1$	W transp. w/o MHD
	aug2417/seq#3	#119	$t_2$	W transp. w/o MHD
	aug2817/seq#1	#120	$t_1$	W transp. w/ MHD
	aug2617/seq#1	#121	$t_2$	W transp. w/ MHD
<b>Simulations with 7b7f3ea091</b>				
4.2	run123_2535_19		$t_1$	default w/ updated $\gamma_{E \times B}$
	run123_5060_58		$t_2$	default w/ updated $\gamma_{E \times B}$
<b>Simulations with 26c9b722e6</b>				
4.2	run123_2535_18		$t_1$	ASTRA-JETTO comparison
	run123_5060_57		$t_2$	ASTRA-JETTO comparison

of the simulation boundary. Simulation results with JETTO-QuaLiKiz version 7b7f3ea091 are found to be in good agreement with experimental observations, similar to simulations under utilization of the previous versions 83e0078788, 8c0622caed and edb9ddab05. In both time slices considered, average disagreement of particle and ion heat transport predictions has changed only by around 0.1% and 1.3%, respectively. Although electron temperature profiles are overpredicted on average by an additional 8.9% in  $t_1$  and 8.0% in  $t_2$ , simulations and experiments still agree within  $1\sigma$  for all profiles predicted. Since experimental observations are thus described with good agreement by the updated version of JETTO-QuaLiKiz, simulations discussed throughout this work are presented as initially performed using previous versions of JETTO-QuaLiKiz.

For the benchmark of the implementation of QuaLiKiz in ASTRA and JETTO, the calculation of the radial electric field in the interface between JETTO and QuaLiKiz (cf. Eq. (6)) was modified to consider the toroidal velocity term only (version 26c9b722e6), thus ensuring identical treatment of the radial electric field in both ASTRA-QuaLiKiz and JETTO-QuaLiKiz. Simulations carried out with this implementation of JETTO-QuaLiKiz are found to be in almost exact agreement with simulations based on the full expression of the radial electric field in version 7b7f3ea091, since the ion pressure profile prescribed is tailored to minimize contributions from  $d^2p_i/dr^2$  to the  $E \times B$  shearing rate. The simulation results presented in Fig. 7 using the reduced expression for  $E_r$  are thus valid for both updated implementations of JETTO-QuaLiKiz, 7b7f3ea091 and 26c9b722e6.

## References

- <sup>1</sup> H. Bolt, V. Barabash, W. Krauss, J. Linke, R. Neu, S. Suzuki, N. Yoshida, and ASDEX Upgrade Team. *J. Nucl. Mater.* **329-333**, 66 (2004).
- <sup>2</sup> R.A. Causey. *J. Nucl. Mater.* **300**, 91 (2002).
- <sup>3</sup> V. Philipps. *J. Nucl. Mater.* **415**, S2 (2011).
- <sup>4</sup> R. Neu, M. Balden, V. Bobkov, R. Dux, O. Gruber, A. Herrmann, A. Kallenbach, M. Kaufmann, C. F. Maggi, H. Maier, H.W. Müller, T. Pütterich, R. Pugno, V. Rohde, A. C. C. Sips, J. Stober, W. Suttrop, C. Angioni, C. V. Atanasiu, W. Becker, K. Behler, K. Behringer, A. Bergmann, T. Bertinelli, R. Bilato, A. Bottino, M. Brambilla, F. Braun, A. Buhler, A. Chankin, G. Conway, D. P. Coster, P. de. Marné, S. Dietrich, K. Dimova, R. Drube, T. Eich, K. Engelhardt, H.-U. Fahrbach, U. Fantz, L. Fattorini, J. Fink, R. Fischer, A. Flaws, P. Franzen, J. C. Fuchs, K. Gál, M. García. Muñoz, M. Gemisic-Adamov, L. Giannone, S. Gori, S. da. Graca, H. Greuner, A. Gude, S. Günter, G. Haas, J. Harhausen, B. Heinemann, N. Hicks, J. Hobirk, D. Holtum, C. Hopf, L. Horton, M. Huart, V. Igochine, S. Kálvin, O. Kardaun, M. Kick, G. Kocsis, H. Kollotzek, C. Konz, K. Krieger, T. Kurki-Suonio, B. Kurzan, K. Lackner, P. T. Lang, P. Lauber, M. Laux, J. Likonen, L. Liu, A. Lohs, K. Mank, A. Manini, M.-E. Manso, M. Maraschek, P. Martin, Y. Martin, M. Mayer, P. McCarthy, K. McCormick, H. Meister, F. Meo, P. Merkel, R. Merkel, V. Mertens, F. Merz, H. Meyer, M. Mlynek, F. Monaco, H. Murmann, G. Neu, J. Neuhauser, B. Nold, J.-M. Noterdaeme, G. Pautasso, G. Pereverzev, E. Poli, M. Püschel, G. Raupp, M. Reich, B. Reiter, T. Ribeiro, R. Riedl, J. Roth, M. Rott, F. Ryter, W. Sandmann, J. Santos, K. Sassenberg, A. Scarabosio, G. Schall, J. Schirmer, A. Schmid, W. Schneider, G. Schramm, R. Schrittwieser, W. Schustereder, J. Schweinzer, S. Schweizer, B. Scott, U. Seidel, F. Serra, M. Sertoli, A. Sigalov, A. Silva, E. Speth, A. Stäbler, K.-H. Steuer, E. Strumberger, G. Tardini, C. Tichmann, W. Treutterer, C. Tröster, L. Urso, E. Vainonen-Ahlgren, P. Varela, L. Vermare, D. Wagner, M. Wischmeier, E. Wolfrum, E. Würsching, D. Yadikin, Q. Yu, D. Zasche, T. Zehetbauer, M. Zilker, and H. Zohm. *Plasma Phys. Control. Fusion* **49**, B59 (2007).
- <sup>5</sup> G.F. Matthews, M. Beurskens, S. Brezinsek, M. Groth, E. Joffrin, A. Loving, M. Kear, M.-L. Mayoral, R. Neu, P. Prior, V. Riccardo, F. Rimini, M. Rubel, G. Sips, E. Villedieu, P. de Vries, M. L. Watkins, and EFDA-JET contributors. *Phys. Scr.* **T145**, 014001 (2011).
- <sup>6</sup> J. Bucalossi, M. Missirlian, P. Moreau, F. Samaille, E. Tsitrone, D. van Houtte, T. Batal, C. Bourdelle, M. Chantant, Y. Corre, X. Courtois, L. Delpech, L. Doceul, D. Douai, H. Dognac, F. Faisse, C. Fenzi,

- F. Ferlay, M. Firdaouss, L. Gargiulo, P. Garin, C. Gil, A. Grosman, D. Guilhem, J. Gunn, C. Hernandez, D. Keller, S. Larroque, F. Leroux, M. Lipa, P. Lotte, A. Martinez, O. Meyer, F. Micolon, P. Mollard, E. Nardon, R. Nouaillietas, A. Pilia, M. Richou, S. Salasca, and J.-M. Travère. *Fusion Eng. Des.* **89**, 907 (2014).
- <sup>7</sup> D.E. Post and R.V. Jensen. *At. Data Nucl. Data Tables* **20**, 397 (1977).
- <sup>8</sup> R. Neu, K. Asmussen, S. Deschka, A. Thoma, M. Bessenrodt-Weberpals, R. Dux, W. Engelhardt, J.C. Fuchs, J. Gaffert, C. García-Rosales, A. Herrmann, K. Krieger, F. Mast, J. Roth, V. Rohde, M. Weinlich, U. Wenzel, ASDEX Upgrade Team, and ASDEX NI-Team. *J. Nucl. Mater.* **241-243**, 678 (1997).
- <sup>9</sup> R. Neu, R. Dux, A. Geier, A. Kallenbach, R. Pugno, V. Rohde, D. Bolshukhin, J.C. Fuchs, O. Gehre, O. Gruber, J. Hobirk, M. Kaufmann, K. Krieger, M. Laux, C. Maggi, H. Murmann, J. Neuhauser, F. Ryter, A.C.C. Sips, A. Stähler, J. Stober, W. Suttrop, H. Zohm, and ASDEX Upgrade Team. *Plasma Phys. Control. Fusion* **44**, 811 (2002).
- <sup>10</sup> R. Dux, C. Giroud, R. Neu, A.G. Peeters, J. Stober, K.-D. Zastrow, Contributors to the EFDA-JET Workprogramme, and ASDEX Upgrade Team. *J. Nucl. mater.* **313-316**, 1150 (2003).
- <sup>11</sup> T. Pütterich, R. Dux, R. Neu, M. Bernert, M.N.A. Beurskens, V. Bobkov, S. Brezinsek, C. Challis, J.W. Coenen, I. Coffey, A. Czarnecka, C. Giroud, P. Jacquet, E. Joffrin, A. Kallenbach, M. Lehnen, E. Lerche, E. de la Luna, S. Marsen, G. Matthews, M.-L. Mayoral, R.M. McDermott, A. Meigs, J. Mlynar, M. Sertoli, G. van Rooij, the ASDEX Upgrade Team, and JET EFDA Contributors. *Plasma Phys. Control. Fusion* **55**, 124036 (2013).
- <sup>12</sup> F.J. Casson, C. Angioni, E.A. Belli, R. Bilato, P. Mantica, T. Odstrcil, T. Pütterich, M. Valisa, L. Garzotti, C. Giroud, J. Hobirk, C.F. Maggi, J. Mlynar, M.L. Reinke, JET EFDA Contributors, and ASDEX Upgrade Team. *Plasma Phys. Control. Fusion* **57**, 014031 (2015).
- <sup>13</sup> C. Angioni. *Phys. Plasmas* **22**, 055902 (2015).
- <sup>14</sup> C. Angioni, R. Bilato, F.J. Casson, E. Fable, P. Mantica, T. Odstrcil, M. Valisa, ASDEX Upgrade Team, and JET Contributors. *Nucl. Fusion* **57**, 022009 (2017).
- <sup>15</sup> C. Angioni, P. Mantica, T. Pütterich, M. Valisa, M. Baruzzo, E.A. Belli, P. Belo, F.J. Casson, C. Challis, P. Drewelow, C. Giroud, N. Hawkes, T.C. Hender, J. Hobirk, T. Koskela, L. Lauro Taroni, C.F. Maggi, J. Mlynar, T. Odstrcil, M.L. Reinke, M. Romanelli, and JET EFDA Contributors. *Nucl. Fusion* **54**, 083028 (2014).
- <sup>16</sup> M. Sertoli, T. Odstrcil, C. Angioni, and the ASDEX Upgrade Team. *Nucl. Fusion* **55**, 113029 (2015).
- <sup>17</sup> M. Sertoli, R. Dux, T. Pütterich, and the ASDEX Upgrade Team. *Plasma Phys. Control. Fusion* **57**, 075004 (2015).
- <sup>18</sup> C. Angioni, M. Sertoli, R. Bilato, V. Bobkov, A. Loarte, R. Ochoukov, T. Odstrcil, T. Pütterich, J. Stober, and the ASDEX Upgrade Team. *Nucl. Fusion* **57**, 056015 (2017).
- <sup>19</sup> M. Sertoli, C. Angioni, R. Dux, R. Neu, T. Pütterich, V. Igochine, and the ASDEX Upgrade Team. *Plasma Phys. Control. Fusion* **53**, 035024 (2011).
- <sup>20</sup> C. Bourdelle, J. Citrin, B. Baiocchi, A. Casati, P. Cottier, X. Garbet, F. Imbeaux, and JET Contributors. Core turbulent transport in tokamak plasmas: bridging theory and experiment with QuaLiKiz. *Plasma Phys. Control. Fusion* **58**, 014036 (2016).
- <sup>21</sup> J. Citrin, C. Bourdelle, F.J. Casson, C. Angioni, N. Bananomi, Y. Camenen, X. Garbet, L. Garzotti, T. Görler, O. Gürçan, F. Koechl, F. Imbeaux, O. Linder, K. van de Plassche, P. Strand, G. Szepesi, and JET Contributors. *Plasma Phys. Control. Fusion* **59**, 124005 (2017).
- <sup>22</sup> G. Cenacchi and A. Taroni. *JETTO: A Free-Boundary Plasma Transport Code*. Rapporto ENEA RT/TIB/88/5, 1988.
- <sup>23</sup> M. Romanelli, G. Corrigan, V. Parail, S. Wiesen, R. Ambrosino, P. da Silva Aresta Belo, L. Garzotti, D. Harting, F. Köchl, T. Koskela, L. Lauro-Taroni, C. Marchetto, M. Mattei, E. Militello-Asp, M.F.F. Nave, S. Pamela, A. Salmi, P. Strand, G. Szepesi, and EFDA-JET Contributors. *Plasma and Fusion Research* **9**, 3403023 (2014).
- <sup>24</sup> S. Breton, F.J. Casson, C. Bourdelle, J. Citrin, Y. Baranov, J. Challis, C. Garcia, G. Corrigan, L. Garzotti, S. Henderson, F. Koechl, M. OMullane, T. Pütterich, M. Sertoli, M. Valisa, and JET contributors. Submitted to *Nucl. Fusion*.
- <sup>25</sup> S. Breton, F.J. Casson, C. Bourdelle, Y. Camenen, J. Citrin, Y. Baranov, C. Challis, J. Garcia, G. Corrigan, L. Garzotti, S. Henderson, F. Koechl, M. O'Mullane, T. Pütterich, M. Sertoli, M. Valisa, and JET contributors. Paper presented at the 44th EPS Conference on Plasma Physics, Belfast, 26-30 June 2017,

- O4.124.
- <sup>26</sup> D. Wagner, J. Stober, F. Leuterer, F. Monaco, M. Münich, D. Schmid-Lorch, H. Schütz, H. Zohm, M. Thumm, T. Scherer, A. Meier, G. Gantenbein, Flamm. J., W. Kasperek, H. Höhnle, C. Lechte, A.G. Litvak, G.G. Denisov, A. Chirkov, L.G. Popov, V.O. Nichiporenko, V.E. Myasnikov, E.M. Tai, E.A. Solyanova, and S.A. Malygin. *J. Infrared Millim. Terahertz Waves* **32**, 274 (2011).
- <sup>27</sup> A. Gude, M. Maraschek, C. Angioni, J. Stober, and the ASDEX Upgrade Team. Paper presented at the 37th EPS Conference on Plasma Physics, Dublin, 21-25 June 2010, P4.124.
- <sup>28</sup> S. Breton, F.J. Casson, C. Bourdelle, C. Angioni, E. Belli, Y. Camenen, J. Citrin, X. Garbet, Y. Sarazin, M. Sertoli, and JET contributors. Submitted to *Phys. Plasmas*.
- <sup>29</sup> A. Ho, J. Citrin, C. Bourdelle, Y. Camenen, F. Felici, M. Maslov, K. van de Plassche, H. Weisen, and JET Contributors. Paper presented at the 44th EPS Conference on Plasma Physics, Belfast, 26-30 June 2017, P5.173.
- <sup>30</sup> M.A. Chilenski, M. Greenwald, Y. Marzouk, N.T. Howard, A.E. White, J.E. Rice, and J.R. Walk. *Nucl. Fusion* **55**, 023012 (2015).
- <sup>31</sup> R.J. Hawryluk. An Empirical Approach to Tokamak Transport. In B. Coppi, G.G. Leotta, D. Pfirsch, R. Pozzoli, and E. Sindoni, *Physics of Plasmas Close to Thermonuclear Conditions*. Pergamon Press, 1981.
- <sup>32</sup> A. Pankin, D. McCune, R. Andre, G. Bateman, and A. Kritz. *Comput. Phys. Commun.* **159**, 157 (2004).
- <sup>33</sup> W.A. Houlberg, K.C. Shaing, S.P. Hirshman, and M.C. Zarnstorff. *Phys. Plasmas* **4**, 3230 (1997).
- <sup>34</sup> M. Erba, V. Parail, E. Springmann, and A. Taroni. *Plasma Phys. Control. Fusion* **37**, 1249 (1995).
- <sup>35</sup> L. Lauro-Taroni, B. Alper, R. Giannella, K. Lawson, F. Marcus, M. Mattioli, P. Smeulders, and M. von Hellermann. *Proc. 21st EPS on Plasma Physics* (1994).
- <sup>36</sup> A. Bock. *Generation and Analysis of Plasma with Centrally Reduced Helicity in Full-Tungsten ASDEX Upgrade*. PhD thesis, Ludwigs-Maximilians-Universität München, 2016.
- <sup>37</sup> C.F. Maggi, E. Delabie, T.M. Biewer, M. Groth, N.C. Hawkes, M. Lehnen, E. de la Luna, K. McCormick, C. Reux, F. Rimini, E.R. Solano, Y. Andrew, C. Bourdelle, V. Bobkov, M. Brix, G. Calabro, A. Czarnecka, J. Flanagan, E. Lerche, S. Marsen, I. Nunes, D. Van Eester, M.F. Stamp, and JET EFDA Contributors. *Nucl. Fusion* **54**, 023007 (2014).
- <sup>38</sup> H. Meyer, E. Delabie, C.F. Maggi, C. Bourdelle, P. Drewelow, I. Carvalho, P. Lang, F. Rimini, and JET EFDA Contributors. Paper presented at the 41st EPS Conference on Plasma Physics, Berlin, 23-27 June 2014, P1.013.
- <sup>39</sup> G.D. Conway. *Plasma Phys. Control. Fusion* **50**, 124026 (2008).
- <sup>40</sup> T. Happel, A. Bañón Navarro, G.D. Conway, C. Angioni, M. Bernert, M. Dunne, E. Fable, B. Geiger, T. Görler, F. Jenko, R.M. McDermott, F. Ryter, U. Stroth, and the ASDEX Upgrade Team. *Phys. Plasmas* **22**, 032503 (2015).
- <sup>41</sup> G.V. Pereverzev and P.N. Yushmanov. *ASTRA - Automated System for TRansport Analysis*. Max-Planck-Institut Für Plasmaphysik, IPP-Report, IPP 5/98, Februray 2002.
- <sup>42</sup> E. Fable, C. Angioni, F.J. Casson, D. Told, A.A. Ivanov, F. Jenko, R.M. McDermott, S.Yu. Medvedev, G.V. Pereverzev, F. Ryter, W. Treutterer, E. Viezzer, and the ASDEX Upgrade Team. *Plasma Phys. Control. Fusion* **55**, 124028 (2013).
- <sup>43</sup> X. Garbet, P. Mantica, C. Angioni, E. Asp, Y. Baranov, C. Bourdelle, R. Budny, F. Crisanti, G. Cordey, L. Garzotti, N. Kirneva, D. Hogewej, T. Hoang, F. Imbeaux, E. Joffrin, X. Litaudon, A. Manini, D.C. McDonald, H. Nordman, V. Prail, A. Peeter, F. Ryter, C. Sozzi, M. Valovic, T. Tala, A. Thyagaraja, I. Voitsekhovitch, J. Weiland, H. Weisen, A. Zabolotsky, and the JET EFDA Contributors. *Plasma Phys. Control. Fusion* **46**, B557 (2004).
- <sup>44</sup> M. Romanelli, C. Bourdelle, and W. Dorland. *Phys. Plasmas* **11**, 3845 (2004).
- <sup>45</sup> S.C. Guo and F. Romanelli. *Phys. Fluids B* **5**, 520 (1993).
- <sup>46</sup> F. Jenko, W. Dorland, and G.W. Hammett. *Phys. Plasmas* **8**, 4096 (2001).
- <sup>47</sup> F. Sommer, J. Stober, C. Angioni, M. Bernert, A. Burckhart, V. Bobkov, R. Fischer, C. Fuchs, R.M. McDermott, W. Suttrop, E. Viezzer, and the ASDEX Upgrade Team. *Nucl. Fusion* **52**, 114018 (2012).
- <sup>48</sup> F. Sommer, J. Stober, C. Angioni, E. Fable, M. Bernert, A. Burckhardt, V. Bobkov, R. Fischer, C. Fuchs, R.M. McDermott, W. Suttrop, E. Viezzer, and the ASDEX Upgrade Team. *Nucl. Fusion* **55**, 033006 (2015).
- <sup>49</sup> E. Fable, C. Angioni, and O. Sauter. *Plasma Phys. Control. Fusion* **52**, 015007 (2010).
- <sup>50</sup> M. Romanelli, G. Regnoli, and C. Bourdelle. *Phys. Plasmas* **14**, 082305 (2007).
- <sup>51</sup> E.A. Belli and J. Candy. *Plasma Phys. Control. Fusion* **50**, 095010 (2008).

- <sup>52</sup> E.A. Belli and J. Candy. *Plasma Phys. Control. Fusion* **54**, 015015 (2012).
- <sup>53</sup> X. Garbet, J.H. Ahn, S. Breton, P. Donnel, D. Esteve, R. Guirlet, H. Lütjens, T. Nicolas, Y. Sarazin, C. Bourdelle, O. Février, G. Dif-Pradalier, P. Ghendrih, V. Grandgirard, G. Latu, J.F. Luciani, P. Maget, A. Marx, and A. Smolyakov. *Synergetic effects of collisions, turbulence and sawtooth crashes on impurity transport*. [hal.archives-ouvertes.fr/hal-01367373](https://hal.archives-ouvertes.fr/hal-01367373) (2016).
- <sup>54</sup> J.H. Ahn, X. Garbet, H. Lütjens, and R. Guirlet. *Dynamics of heavy impurities in non-linear MHDS simulations of sawtooth tokamak plasmas*. [hal.archives-ouvertes.fr/hal-01340291](https://hal.archives-ouvertes.fr/hal-01340291) (2016).
- <sup>55</sup> T. Nicolas, R. Sabot, X. Garbet, H. Lütjens, J.F. Luciani, Z. Guimaraes-Filho, J. Decker, and A. Merle. *Phys. Plasmas* **19**, 112305 (2012).
- <sup>56</sup> T. Nicolas, H. Lütjens, J.F. Luciani, X. Garbet, and R. Sabot. *Phys. Plasmas* **21**, 012507 (2014).